Vibrational Properties of the Organometal Halide Perovskite $CH_3NH_3PbI_3$ from Theory and Experiment: Factor Group Analysis, First-Principles Calculations, and Low-Temperature Infrared Spectra

Miguel A. Pérez-Osorio,[†] Rebecca L. Milot,[‡] Marina R. Filip,[†] Jay B. Patel,[‡] Laura M. Herz,[‡] Michael B. Johnston,[‡] and Feliciano Giustino[*,†]

Department of Materials, University of Oxford, Parks Road, Oxford, OX1 3PH, UK, and Clarendon Laboratory, Department of Physics, University of Oxford, Parks Road, OX1 3PU, Oxford, UK

[*]To whom correspondence should be addressed
[†]Department of Materials, University of Oxford, Parks Road, Oxford, OX1 3PH, UK
[‡]Clarendon Laboratory, Department of Physics, University of Oxford, Parks Road, OX1 3PU, Oxford, UK

Abstract

In this work we investigate the vibrational properties of the hybrid organic/inorganic halide perovskite $MAPbI_3$ ($MA{=}CH_3NH_3$) in the range 6–3500 cm^{-1} by combining first-principles density-functional perturbation theory calculations and low-temperature infrared (IR) absorption measurements on evaporated perovskite films. By using a group factor analysis we establish the symmetry of the normal modes of vibration and predict their IR and Raman activity. We validate our analysis via explicit calculation of the IR intensities. Our calculated spectrum is in good agreement with our measurements. By comparing theory and experiment we are able to assign most of the features in the IR spectrum. Our analysis shows that the IR spectrum of $MAPbI_3$ can be partitioned in three distinct regions: the internal vibrations of the MA cations (800−3100 cm^{-1}), the cation librations (140−180 cm^{-1}), and the internal vibrations of the PbI_3 network (< 100 cm^{-1}). The low-frequency region of the IR spectrum is dominated by Pb−I stretching modes of the PbI_3 network with B_u symmetry and librational modes of the MA cations. In addition, we find that the largest contributions to the static dielectric constant arise from Pb−I stretching and Pb−I−Pb rocking modes, and that one low-frequency B_{2u} Pb-I stretching mode exhibits a large LO-TO splitting of 50 cm^{-1}.

1 Introduction

Solar cells based on methylammonium lead tri-iodide, $MAPbI_3$ with $MA = CH_3NH_3^+$, have attracted the attention of the photovoltaic research community due to the unprecedented rate of improvement in their performance. The highest certified power conversion efficiency of these devices has recently reached the record of 20.1%.[1] $MAPbI_3$ was introduced as a light sensitizer in dye-sensitized solar cells and meso-superstructured solar cells.[2–4] Subsequently it was realized that $MAPbI_3$ can also act as the electron or hole conductor in planar heterojunction cells.[5–11] These breakthroughs enabled the development of solar cells employing metal halide perovskites which are suitable for low-temperature processing,[7,12–15] are transparent,[16,17] and can be produced in various colours,[16,18–20] to the point that they already constitute a very promising technology.[21]

$MAPbI_3$ is a semiconductor with a direct band gap of 1.5-1.6 eV,[22,23] which is ideal for absorbing light in the visible range. Upon photoexcitation, electron-hole pairs rapidly dissociate at room temperature, leading to free carriers.[23] The carriers exhibit diffusion lengths as high as 1 μm,[24–27] therefore electron extraction from $MAPbI_3$ is very efficient.[25] $MAPbI_3$ crystallizes in a perovskite structure of the AMX_3 type,[28] where the Pb and I atoms occupy the M and X sites, respectively. The structure consists of PbI_6 corner-sharing octahedra, which define a cuboctahedral cavity occupied by the MA cations (Fig. 1). At low temperature (below 162.2 K) $MAPbI_3$ crystallizes in an orthorhombic *Pnma* structure; between 162.2 K and 327.4 K the structure is tetragonal ($I4/mcm$), and above 327.4 K the system stabilizes in a cubic phase.[22,29–32] While the configuration of the MA cations is well defined in the low-temperature orthorhombic phase, there exists a considerable degree of angular fluctuations in the tetragonal and cubic phases.[22,30,32] Weller et al.[29] report a neutron powder diffraction study of $MAPbI_3$ as a function of temperature, which clearly shows an increase in the angular disorder of MA with temperature. Computational studies of $MAPbI_3$ confirm that changes in the cation orientation only involve variations in the total energy of a few meV per formula unit,[33–39] in line with the above experimental observations.

A good understanding of the vibrational modes in $MAPbI_3$ is highly relevant for understanding the optoelectronic properties of these materials. For instance Wehrenfennig et al.[40] recently showed that luminescence from this materials exhibits significant homogeneous broadening as a result of strong phonon coupling. The vibrational properties of $MAPbI_3$ have been investigated by several

research groups.[41–45] Quarti et al.[41] have performed a Raman study of $MAPbI_3$ at room temperature in the spectral range from 50 to 450 cm^{-1}. They identified three sharp peaks at 62, 94 and 119 cm^{-1}, and one broad feature around 250 cm^{-1}. These peaks were assigned respectively to bending of the Pb−I−Pb bonds; stretching of the Pb−I bonds and libration of the MA cations; libration of the MA cations; torsion of the MA cations. More recently Ledinsky et al.[42] also measured the Raman spectrum of $MAPbI_3$ in the range 50-700 cm^{-1}, although the broad feature around 250 cm^{-1} and the peak at 94 cm^{-1} were not observed. In order to explain this discrepancy the authors suggested that these two features reported by Quarti et al.[41] relate to PbI_2 species formed as a result of sample degradation. Onoda-Yamamuro et al.[43] reported the infrared (IR) absorption spectrum of $MAPbI_3$ in the range 850-1000 cm^{-1}, measured at various temperatures between 140 K and 299 K. The authors assigned the observed spectral features by comparison with the IR spectra of known compounds. More recently IR measurements were reported by Mosconi et al.[44] over the range 30-500 cm^{-1} at various temperatures (between 180 K and 293 K), and by Glaser et al.[45] from 700 to 3700 cm^{-1} at room temperature. By comparing the measured spectra to calculations for an isolated $CH_3NH_3^+$ cation, Glaser et al.[45] assigned the IR peaks above 900 cm^{-1} to internal vibrations of MA.

Two computational studies addressed the vibrational properties of $MAPbI_3$.[41,44] In both works the authors extracted the vibrational spectra by performing density functional perturbation theory calculations. These studies succeeded in achieving a good qualitative agreement with the experiment, however a detailed group-theoretical analysis of the vibrational modes, a prediction of Raman and IR activities of each normal mode, and the assignment of the measured peaks to specific vibrations are still missing. Given the growing importance of $MAPbI_3$ as photovoltaic and optoelectronic material, a systematic investigation of these aspects is warranted.

In this work we perform a systematic study of the vibrational properties of $MAPbI_3$ in the low-temperature orthorhombic phase by combining first-principles calculations and IR measurements on polycrystalline samples obtained by vacuum evaporation. We provide a comprehensive group-theoretical analysis of the normal modes of vibration, and we predict the IR and Raman activity of each mode based on symmetry considerations. In order to validate our analysis we calculate the IR intensities using the standard Born effective charges. By comparing theory and experiment we are able to assign almost every spectral feature. Finally we also discuss the static dielectric properties

of $MAPbI_3$ and identify the vibrational modes which dominate the screening at low frequency.

The present work provides a detailed study of the infrared spectrum of the low-temperature phase of the $MAPbI_3$ perovskite, and our results can be used as a solid reference for the characterization of this perovskite (IR spectroscopy offers high resolution over a wide range of frequencies and short measurement times).[46] For instance, by analyzing the infrared spectrum of a material one can study defect concentration, dielectric properties, heat capacities, charge carrier densities and relaxation rates.[43,45,47,48] The determination of these properties in the low-temperature phase is crucial to achieve a complete understanding of the outstanding performance of the technologically relevant phase of the $MAPbI_3$ (room-temperature phase). In addition, our results can also be used as a reference in the study of the phase transitions and degradation processes in $MAPbI_3$.[43]

The manuscript is organized as follows: in Sec. 2 we introduce the computational and experimental methods. In Sec. 3 we discuss the results of our calculations, with an emphasis on the normal modes of vibration (Sec. 3.2), the Born dynamical charges (Sec. 3.5), and the IR spectrum of $MAPbI_3$ (Sec. 3.6). For completeness in Sec. 3.4 we also analyze the sensitivity of our calculated vibrational frequencies to the choice of the DFT functional and the inclusion of relativistic effects and van der Waals interactions. In Sec. 4 we compare theory and experiment and assign the spectral features. In particular, in Sec. 4.1 we discuss the relevance of our findings for the room-temperature tetragonal phase of $MAPbI_3$, and in Sec. 4.2 we discuss the LO-TO splitting in this compound. In Sec. 5 we summarize our findings and offer our conclusions.

2 Methodology

2.1 Computational methods

We calculate the normal modes of $MAPbI_3$ in the *Pnma* orthorhombic structure, since in this phase the sublattice formed by the MA cations has been fully resolved via X-ray diffraction measurements.[22] The study of lattice dynamics in the two high-temperature phases, where the MA cations can rotate, would require averaging over several possible orientations of the MA cations, and are best addressed using molecular dynamics simulations.[41,44]

We study structural properties using DFT and vibrational properties using density functional perturbation theory (DFPT) as implemented in the `Quantum ESPRESSO` suite.[49] Most calculations

are based on the local density approximation (LDA) to the exchange and correlation energy.[50,51] In Sec. 3.4 we also employ the PBE generalized gradient approximation for our sensitivity analysis.[52] The core-valence interaction is described by means of ultrasoft pseudo-potentials.[53] The electron wavefunctions and charge density are represented using planewaves basis sets with kinetic energy cutoff of 40 Ry and 200 Ry, respectively. The Brillouin zone is sampled using a 4×4×4 Monkhorst-Pack grid. The atomic positions are optimized until the largest force is smaller than 0.01 eV/Å, using the experimental lattice parameters.[22] In Sec. 3.4 we also discuss calculations performed using optimized lattice parameters. In all cases the structural optimization is initialized using the experimental coordinates of the Pb, I, C, and N atoms.[22] The H atoms of the MA cations (not resolved in experiment) are introduced using the geometry of the MA cation and the *Pnma* symmetry. In Sec. 3.4 we also investigate the effects of van der Waals corrections using the formalism proposed by Grimme et al.[54] and Barone et al.[55]

Given the relatively large unit cell, we calculate the normal vibrational modes within the harmonic approximation at the Γ point. The LO-TO splitting (to be discussed in Sec. 4.2) is taken into account by evaluating the non-analytic term of the dynamical matrix.[56] The Born effective charge tensors[57] are calculated as variations of the macroscopic electric polarization with respect to the displacement of atomic sublattices, using the modern theory of polarization:[58]

$$Z^*_{\kappa,\alpha\beta} = \frac{\Omega}{e}\frac{\partial P_\alpha}{\partial u_{\kappa\beta}}, \tag{1}$$

where κ labels the atoms in the unit cell, α and β indicate Cartesian directions, Ω is the unit cell volume, and e is the electron charge. $\mathbf{P}$ is the macroscopic polarization (dipole per unit cell) and $\mathbf{u}_\kappa$ an atomic displacement from equilibrium. We note that $Z^*_{\kappa,\alpha\beta}$ is by definition dimensionless. It is convenient to define the dimensionless effective charge vectors $Z^*_{\alpha\nu}$ for each vibrational eigenmode ν as follows:

$$Z^*_{\alpha\nu} = \sum_{\kappa\beta} \sqrt{\frac{M_0}{M_\kappa}} e_{\kappa\beta,\nu} Z^*_{\kappa,\alpha\beta}, \tag{2}$$

where M_κ are the nuclear masses, M_0 is the average mass over the unit cell, and $e_{\kappa\beta,\nu}$ are the vibrational eigenmodes with frequency ω_ν. Using this definition the real part of the frequency-

dependent (transverse) macroscopic dielectric function in the infrared range is given by:[56]

$$\epsilon_1(\omega) = \epsilon_1^{\infty} + \frac{e^2}{4\pi\varepsilon_0}\frac{4\pi}{3\Omega}\frac{1}{M_0}\sum_{\alpha\nu}\frac{|Z^*_{\alpha\nu}|^2}{\omega_\nu^2 - \omega^2}, \tag{3}$$

where ϵ_∞ is the high-frequency permittivity arising from electronic interband transitions, ε_0 is the vacuum permittivity, and the factor of 1/3 comes from the isotropic average. In this work we calculate the high-frequency dielectric constant using finite electric fields.[59,60]

The IR spectrum is proportional to $\omega\epsilon_2(\omega)$ where ϵ_2 is the imaginary part of the dielectric function. Therefore we define the IR intensity as follows:

$$I(\omega) = \frac{e^2}{M_0}\sum_{\alpha\nu}|Z^*_{\alpha\nu}|^2\delta(\omega - \omega_\nu) \propto \omega\epsilon_2(\omega). \tag{4}$$

In our calculations we replace the Dirac delta functions by Gaussians with a broadening of 5 cm^{-1}.

2.2 Experimental methods

Dual-source thermal evaporation[6,61] was used to grow thin films of $MAPbI_3$ on three different types of substrate to enable transmission measurements to be performed in the range 6–3500 cm^{-1}. KBr, high resistivity silicon and z-cut quartz substrates were used for measurements in the near and mid infrared, far infrared and terahertz frequencies regions of the spectrum, respectively. Prior to the evaporation, the tooling factor was determined by depositing the starting powders, PbI_2 and methylammonium iodide ($MAI = CH_6IN$) separately and then measuring the layer thicknesses. MAI was synthesized using previously reported methods.[4] Lead(II) iodide, ultra dry, 99.999% (metals basis) was purchased from Alfa Aesar.

MAI and PbI_2 (300 mg of each) were placed in the separate crucibles, and the various substrates were mounted on a rotating substrate holder to ensure that a uniform film was deposited. The temperature of the substrates was kept at 21°C throughout the deposition. The chamber was allowed to reach a high vacuum (10^{-6} mbar), before heating the PbI_2 to 250°C; once the rate was stabilized the MAI was heated to 100°C. Once the deposition rate for MAI had stabilized the substrates were exposed to the vapor. The rates of both the MAI and PbI_2 were monitored using a quartz crystal microbalance to ensure a 1:1 molar ratio was achieved in the final composition of the

film. The final deposition rate was 0.8 Å s^{-1} and the thickness of the films were 390 nm (DEKTAK 150 profiler). The films were annealed at 100°C for 15 minutes followed by 5 minutes at 150°C.

The experimental vibrational spectrum from 60 to 3500 cm^{-1} was measured with a Bruker Vertex 80v Fourier-transfer infrared (FTIR) spectrometer with a globar source. A liquid-nitrogen-cooled photovoltaic HgCdTe detector was used to detect the spectral range from 680 to 3500 cm^{-1}, and the spectrum in the far infrared (60–680 cm^{-1}) was measured with a silicon bolometer (Infrared Laboratories Inc), which was cooled with liquid helium. Mylar and KBr beamsplitters were used to cover the spectral range 60–300 cm^{-1} and 300-3500 cm^{-1}, respectively. To measure the spectrum from 6–60 cm^{-1}, terahertz time-domain spectroscopy (THz-TDS) was used. The THz-TDS setup has been described elsewhere;[62] it consisted of an amplified laser system (Mai Tai - Empower - Spitfire Pro from Spectra Physics), which was used to generate THz radiation via optical rectification in a GaP(110) single crystal and detect it via electrooptic sampling in an 0.2 mm thick GaP(110) crystal and a pair of balanced photodiodes. For both THz and FTIR measurements, the samples were mounted on the cold finger of a cryostat (MicrostatHe, Oxford Instruments) and cooled with liquid helium to 10 K. All spectra were recorded in transmission geometry and referenced to the appropriate bare substrate.

3 Vibrational properties: calculations

3.1 Structure

Figure 1 shows a polyhedral model of the optimized orthorhombic structure of $MAPbI_3$, with the Pb atoms (black spheres) located at the center of the octahedra, and the I atoms (purple spheres) at the corners. The octahedra are connected in a corner-sharing configuration. The MA cations are located inside the cuboctahedral cages defined by the Pb and I atoms (i.e. the A site of standard ABX_3 perovskites) with the C-N axis almost parallel to either the [101] or the $[\bar{1}01]$ directions in the conventional unit cell.

The primitive unit cell contains four $MAPbI_3$ formula units, that is 48 atoms. The optimized Pb-I bond length is 3.19 Å, and the apical and equatorial Pb-I-Pb angles are 158.7° and 149.5°, respectively. These values compare well with the experimental values of 3.18 Å, 161.9° and 150.7°, respectively. In the case of the MA cations, the C-H, N-H, and C-N bond lengths are 1.10, 1.05,

and 1.46 Å, respectively. The corresponding experimental values are 1.1, 1.0, and 1.57 Å. The calculations of vibrational frequencies in Sec. 3.4 using optimized lattice parameters are performed using $a = 8.6821$ Å, $b = 12.3661$ Å, and $c = 8.3016$ Å. These parameters are all within 3% from the corresponding experimental values.[22]

3.2 Decomposition of the normal modes of vibration

Figure 2(a) shows that the frequency range of the calculated vibrational modes of $MAPbI_3$ extends up to 3100 cm^{-1}. We have 144 normal modes, corresponding to the number of degrees of freedom of 4 $CH_3NH_3PbI_3$ units in our unit cell. Visual inspection of the atomic displacements for each mode allows us to identify vibrations of the PbI_3 network, vibrations of the MA cations, as well as mixed modes. Furthermore, some modes can be described as the rigid-body motion of PbI_6 octahedra or MA cations. In order to *quantify* these observations we perform a systematic decomposition of each vibrational mode by defining appropriate projection operations as follows.

First we establish the cation (MA) and network (PbI_3) component of each vibrational mode by simply projecting the vibrational eigenstates onto the Cartesian displacements of the respective atoms. The weights of all MA and PbI_3 components correctly adds up to $4 \times 8 \times 3 = 96$ and $4 \times 4 \times 3 = 48$ degrees of freedom, respectively, as expected. After this initial decomposition, we focus on the component of each mode which belongs to the MA cations, and we proceed to decomposing the atomic displacements into the following components: (i) rigid translations, (ii) spinning around the C−N axis, (iii) libration around the center of mass, and (iv) internal vibrations. To this aim we write the displacement of each atom κ for each vibrational mode ν as follows:

$$\Delta\boldsymbol{\tau}_{\kappa,\nu} = \Delta\boldsymbol{\tau}^{\mathrm{tr}}_{\kappa,\nu} + \Delta\boldsymbol{\tau}^{\mathrm{spin}}_{\boldsymbol{\kappa},\boldsymbol{\nu}} + \Delta\boldsymbol{\tau}^{\mathrm{libr}}_{\kappa,\nu} + \Delta\boldsymbol{\tau}^{\mathrm{int}}_{\kappa,\nu}. \tag{5}$$

We now proceed to determine each of these components in turn: (i) For determining the MA translations we calculate the coordinates of the center of mass of each cation in the equilibrium geometry, $\boldsymbol{\tau}^{(1)}_{\mathrm{CM}}$, and in the configuration with the vibrational eigenmode frozen-in, $\boldsymbol{\tau}^{(2)}_{\mathrm{CM}}$. We note that the definition of center of mass requires us to consider the real atomic displacements as opposed to the mass-scaled displacements. The vector $\Delta\boldsymbol{\tau}^{\mathrm{tr}}_{\kappa,\nu} = \boldsymbol{\tau}^{(2)}_{\mathrm{CM}} - \boldsymbol{\tau}^{(1)}_{\mathrm{CM}}$ defines the translational component of a given MA cation in this vibrational mode. (ii)-(iii) The next step is to remove the translational

component from every atomic displacement: we define the atomic displacement *without* translation as $\Delta\boldsymbol{\tau}'_{\kappa,\nu} = \Delta\boldsymbol{\tau}_{\kappa,\nu} - \Delta\boldsymbol{\tau}^{\mathrm{tr}}_{\kappa,\nu}$, and we proceed to extract the rotations from $\Delta\boldsymbol{\tau}'_{\kappa,\nu}$. In this case we choose the three orthogonal rotations axes so as they intersect at the center of mass of the cation, and one axis is taken along the C−N bond. The rotational component along the C−N bond is the 'spinning', and the other two components around axes perpendicular to the C−N bond correspond to 'librations'. For each rotation axis $\mathbf{n}$ we evaluate the momentum of inertia I using the atomic coordinates and masses, and the angular momentum L along the rotation axis using the atomic masses and displacements $\Delta\boldsymbol{\tau}'_{\kappa,\nu}$ (the choice of the time interval is inconsequential). From these two quantities we calculate the average rotation frequency of the MA cation through the relation $L = I\omega$. The component of the atomic displacement arising from this rigid-body rotation is then found as $\Delta\boldsymbol{\tau}^{\mathrm{rot},\mathbf{n}}_{\kappa,\nu} = \mathbf{n}\,\omega \times \boldsymbol{\tau}_{\kappa}$. (iv) The internal vibrations of the cations are simply obtained by removing the rotational components from what is left of the atomic displacements: $\Delta\boldsymbol{\tau}^{\mathrm{int}}_{\kappa,\nu} = \Delta\boldsymbol{\tau}'_{\kappa,\nu} - \Delta\boldsymbol{\tau}^{\mathrm{spin}}_{\kappa,\nu} - \Delta\boldsymbol{\tau}^{\mathrm{lib}}_{\kappa,\nu}$.

For the vibrational modes of the PbI_6 octahedra we perform a decomposition into rigid translations, rotations, and internal vibrations using the same procedure as outlined above for the cations. The only differences are that for convenience we set the three orthogonal rotation axes to coincide with the unit cell vectors, and we assign each I atom to two PbI_6 octahedra with equal weights.

These steps allow us to decompose each atomic displacement as $\Delta\boldsymbol{\tau}_{\kappa,\nu} = \sum_n \Delta\boldsymbol{\tau}^{(n)}_{\kappa,\nu}$, where n is a short to indicate the translations, rotations, and internal modes of either MA cations or PbI_6 octahedra. The fraction of each component in a given mode is then obtained as

$$f_n = \frac{\sum_\kappa M_\kappa \left|\Delta\boldsymbol{\tau}^{(n)}_{\kappa,\nu}\right|^2}{\sum_n \sum_\kappa M_\kappa \left|\Delta\boldsymbol{\tau}^{(n)}_{\kappa,\nu}\right|^2}, \tag{6}$$

where the nuclear masses M_κ are necessary in order to switch to the orthonormal mass-scaled vibrational eigenmodes. We note that the denominator in this expression is in general different from 1 (even though the eigenmodes are normalized, that is $\sum_\kappa M_\kappa \left|\Delta\boldsymbol{\tau}_{\kappa,\nu}\right|^2 = 1$). This is a consequence of the fact that the basis used for the decomposition is not orthogonal. Using an orthogonal basis is possible in principle, but this would result into mixing translational and rotational components and hence would defy the purpose of this analysis. As a sanity check we verified the deviation

from orthogonality: in most cases the denominator in Eq. (6) deviates from unity by less than 3%. However, in the case of the modes identified as rotations of the PbI_6 octahedra (brown sticks in Fig. 1), this deviation can reach up to 40% since the Pb-I-Pb bending and the PbI_6 rotations define overlapping subspaces. In practice this does not affect any of our conclusions, as it merely changes the fraction of 'rotation' that we identify in such modes.

As a further test we checked that by adding up the components of the MA cation for each mode we correctly obtain 12 translations, 8 librations, 4 spins, and 72 internal vibrations, respectively. Similarly for the PbI_3 network the sum of the contributions yield 3 translations, 2 rotations, and 43 internal vibrational modes. The fact that we obtain only 2 independent rotations is in good agreement with the platonic model of *Pnma* perovskites developed by Filip et al.[63] We also perform a similar quantitative analysis to establish the contribution of the Pb−I stretching, Pb−I−Pb bending and Pb−I−Pb rocking to the vibrational modes of the PbI_3 network.

The result of this decomposition is shown in Figures 2 and 3. In the former we show the contributions of translation, rotation, and internal modes of MA and PbI_3 to each vibrational mode, in order of increasing energy. In the latter we have the total and partial vibrational density of states (vDOS) obtained from this analysis. The normal modes with frequencies between 300 and 3200 cm^{-1} are exclusively internal vibration of the MA cations, i.e. torsion, stretching and bending modes of the C−H, N−H and C−N bonds, and are represented in green in Fig. 2(b) (modes 73–144) and Fig. 3. Below 200 cm^{-1} we find 48 normal modes corresponding mostly ($> 80\%$) to internal vibrations of the PbI_3 network. These modes are represented in blue. Four normal modes with very large contribution arising from MA spinning are found between 100–150 cm^{-1} (yellow). The remaining modes are identified with a mix of MA translations (black) and librations (red), and appear in the frequency range 5–200 cm^{-1}.

From Fig. 2(b) we can see that the mixing between the *internal* vibrational modes of the PbI_3 network and those of the MA cation is negligible. This observation suggests that we can proceed with the symmetry analysis of these modes by considering the perovskite network and the MA cations as separate entities. This analysis is presented in the next section.

3.3 Symmetry analysis

3.3.1 Vibrations of the PbI_3^- network

In order to clarify the symmetry and predict the IR and Raman activity of each vibrational mode we proceed to a factor group analysis.[64] For the PbI_3 network we consider the symmetry operations of the *Pnma* space group (D_{2h}^{16}). The PbI_3 network of $MAPbI_3$ admits 48 vibrational modes at Γ, including 3 pure translations and 45 optical modes. The optical modes can be classified using the following symmetry representation:

$$\Gamma = \underbrace{7B_{1u} + 6B_{2u} + 7B_{3u}}_{\text{IR active}} + \underbrace{5A_g + 4B_{1g} + 5B_{2g} + 4B_{3g}}_{\text{Raman active}} + 7A_u. \quad (7)$$

In order to identify the representation of each mode we verified the associated character tables by directly applying the appropriate symmetry operations to each displacement pattern.[64] The representation and frequency of each mode are shown in Table 1, and schematic representations of characteristic normal modes are provided in Fig. 4.

Based on the symmetry properties of the normal modes we can predict which vibrations will be IR active or Raman active using the matrix element theorem.[65] For a mode to be IR active it is necessary that the eigenmode belongs to one of the irreducible representations of the electric dipole operator. In the case of orthorhombic $MAPbI_3$ the representation of the dipole is $B_{1u} \oplus B_{2u} \oplus B_{3u}$,[64] therefore the B_{1u}, B_{2u}, and B_{3u} modes will be IR-active. This justifies our assignment in Eq. (7).

In the case of the Raman spectrum a mode will be active if the displacement pattern belongs to one of the irreducible representations of the polarizability tensor. In the case of orthorhombic $MAPbI_3$ the polarizability is represented as $B_{1g} \oplus B_{2g} \oplus B_{3g} \oplus A_g$,[64] therefore all the modes of symmetry B_{1g}, B_{2g}, B_{3g} and A_g normal modes are expected to be Raman-active. This is indicated in Eq. (7). The remaining A_u normal modes in Eq. (7) are expected to be silent, as their irreducible representation is not contained neither in the dipole nor in the polarizability representations. In Table 1 we report the calculated vibrational frequencies of each mode, together with the labels 'IR' or 'R' to indicate whether the mode is expected to be IR- or Raman-active. This table contains the TO frequency of the normal modes. In order to confirm our predictions we explicitly calculate

the IR intensities of the normal modes, and we report our results in Table 1. More details on these calculations will be provided in Sec. 3.6 below. Our *ab initio* calculations confirm indeed that the B_u modes are mostly IR active, and that all other modes exhibit a negligible IR activity (≤ 0.1 $\mathrm{D}^2/\mathrm{\AA}^2\,\mathrm{amu}$).

Although we do not explicitly calculate the Raman intensity of the normal modes, we can compare our symmetry analysis with the Raman spectra recently reported by Ledinsky et al.[42] These authors identified Raman signal in the spectral region from 20 to 700 cm^{-1}, and found two distinct peaks at 52 and 110 cm^{-1}. These findings match our analysis, which yield Raman-active A_g and B_g modes in the same frequency range (Table 1).

3.3.2 Internal vibrations of the $CH_3NH_3^+$ cations

In order to analyze the internal vibrations of the MA cations we use the symmetry representations of the C_{3v} point group. Before considering the vibrational modes of MA in $MAPbI_3$ we perform preliminary calculations for the $CH_3NH_3^+$ cation in isolation, to be used as a guideline to assign the modes in the crystal. In this case the calculations are performed in a large cubic supercell and the positive charge is compensated by a uniform negative background. The factor group analysis of the internal modes of MA yield the representations $A_2 + 5A_1 + 6E$, with the E modes doubly degenerate.

In the case of $MAPbI_3$ we find the same irreducible representations, multiplied by a factor of 4 as there are 4 MA units in the orthorhombic cell. The frequencies calculated for the bulk $MAPbI_3$ are reported in Table 2. For simplicity we only report the average of the frequencies for modes belonging to the same irreducible representation.

Using the same procedure as in Sec. 3.3.1 we can predict the IR and Raman activity of the cations based on symmetry considerations. We find that the A_1 and E modes are both IR and Raman active. In contrast, the A_2 modes are silent. These predictions are confirmed by our calculated IR intensities, as shown in Table 2.

3.3.3 Rigid-body motion of the $CH_3NH_3^+$ cations

Besides vibrational modes that can be analyzed using the factor group analysis by considering the PbI_3 network and the MA cations separately, in Fig. 1 we see additional vibrational modes which

corresponds to the rigid-body motion of the cations. These modes are mostly concentrated in the frequency range 0–200 cm^{-1} as it can be seen in the partial vDOS, Fig. 2. In particular we have cation translation and libration modes peaking around ∼90 cm^{-1} and ∼160 cm^{-1}, and spinning modes around ∼130 cm^{-1}. In Table 3 we report the frequency of each of these normal modes, along with the calculated IR intensities (in this case we do not use symmetry to predict IR and Raman activity). Figure 5 shows schematic representations of the normal modes with the highest IR intensities.

3.4 Sensitivity analysis for vibrational frequencies

The accuracy of the calculated vibrational frequencies rests upon the quality of the description of the underlying DFT electronic screening. In the case of $MAPbI_3$ it is known that the band gap calculated within scalar-relativistic DFT is in apparent agreement with experiment,[34] however this is an artifact arising from the neglect of spin-orbit interactions. In order to correctly describe the band gap of $MAPbI_3$ within a fully-relativistic framework it is important to include *GW* quasiparticle corrections.[63,66–69] The most accurate calculations yield a bandgap of 1.7 eV, in good agreement with experiment.[63] Since calculations of vibrational spectra within the *GW* formalism is still beyond current capabilities, we have chosen to perform calculations using scalar-relativistic (sc) DFT/LDA on the grounds that the sc-LDA band gap is (fortuitously) very close to that obtained within fully relativistic *GW* calculations. This should ensure that the dielectric screening and hence the vibrational frequencies are well described in our calculations. In order to check this point, we investigate the effect of the exchange-correlation functional and spin-orbit coupling on the calculated frequencies. For completeness, we also check the effect of using optimized lattice parameters and including van der Waals interactions.

Since the calculation of the force constant matrix is computationally demanding, instead of re-computing all vibrational eigenfrequencies, we adopt a perturbative approach whereby the eigenmodes are taken from our initial sc-LDA calculation. In this approach we map the parabolic minimum of the DFT total energy along a given normal mode coordinate x_ν and obtain the corresponding eigenfrequency ω_ν as the second derivatives of the total energy $E_{\rm tot}$ with respect to this coordinate: $\omega_\nu^2 = M_0^{-1}\partial^2 E_{\rm tot}/\partial x_\nu^2$. The atomic displacements corresponding to the normal mode coordinate x_ν are generated using $\Delta\tau_{\kappa\alpha} = (M_0/M_\kappa)^{1/2} e_{\kappa\alpha,\nu} x_\nu$, where $e_{\kappa\alpha,\nu}$ is the same as in

Eq. (2).[70]

The computed total energy curves corresponding to some representative normal modes are shown in Fig. 6. For clarity we consider the B_{3g} internal mode of the PbI_3 network at 106.9 cm^{-1}, the libration mode of the MA cations at 165.8 cm^{-1}, and the A_1 internal mode of the MA cation at 1418 cm^{-1}. The total energy curves are for our initial sc-LDA calculations, for relativistic LDA, for LDA including van der Waals interactions, for LDA with optimized lattice parameters, and for the PBE generalized gradient approximation.[52] As expected the qualitative picture remains unchanged in all cases. The calculated vibrational frequencies are reported in Table 4. From this table we see that the use of experimental or optimized lattice parameters leads to a small change of at most 10 cm^{-1} in the calculated frequencies. The inclusion of van der Waals interactions reduces significantly the frequencies of the PbI_3 network and librations of the MA cations by as much as 30 cm^{-1}, indicating that the interaction between the H atoms of the MA cations and the PbI_3 network affects the low-frequency vibrations of the $MAPbI_3$ perovskite. We will further discuss this result in Sec. 4 where we compare our theoretical IR spectrum for the $MAPbI_3$ with our experimental data. The inclusion of relativistic corrections reduces the frequency of the PbI_3 network and libration of the MA cations by 15 cm^{-1}, while the internal vibrations of the MA cations are practically unchanged. We regard the relatively large discrepancy between scalar relativistic and relativistic LDA for the B_{3g} internal mode of the PbI_3 network and the libration mode of the MA cations as an artifact arising for the severe underestimation of the band gap in SOC-LDA, and we expect that the scalar-relativistic value to be more reliable. When moving from LDA to PBE we find a change in the PbI_3 frequencies of at most 10 cm^{-1}, and up to 50 cm^{-1} for the high-frequency stretching vibrations of the cation. As we will see in Sec. 3.6 this shift fully accounts for the discrepancy between our calculations and our measured IR spectra at high frequency.

3.5 Born effective charges

The calculated Born effective charge tensor [Eq. (1)] of the Pb atoms are found to be almost diagonal and isotropic. The isotropic average is $(1/3)\sum_\alpha Z^*_{\alpha\alpha} = +4.42$, the largest deviation from this value along the diagonal is 0.1, and the largest off-diagonal element is 0.77. Interesting the Born charge of Pb is significantly larger than the nominal ionic charge +2. This finding is in line with similar observations made for oxide perovskites,[71,72] and indicates that these compounds have a mixed

covalent-ionic bonding character.

In the case of the I atoms the calculated effective charge tensors are highly anisotropic, even after rotating the reference frame to be aligned with the nearest-neighbor Pb-Pb directions. In this frame the largest off-diagonal component is 0.18, and the diagonal elements are (in average) -4.15, -0.77, and -0.72. The largest component is always along the direction of the Pb-I bonds, as expected. The isotropic average of the Born charges of I the atoms is -1.88, considerably larger that the nominal charge of -1. This finding is consistent with the observation made in the case of Pb, confirming the mixed character of the bonding.

For the MA cations we only discuss the isotropic averages of the Born charges. In the case of carbon and nitrogen we find $(1/3)\sum_\alpha Z^*_{\alpha\alpha,\mathrm{C}} = +0.03$ and $(1/3)\sum_\alpha Z^*_{\alpha\alpha,\mathrm{N}} = -0.95$, respectively. The hydrogen atoms associated with C and N carry effective charges +0.13 and +0.55, respectively. If we take the sum of the (isotropic components) of the Born charges for $-CH_3$ and for $-NH_3$ separately we find +0.42 and +0.70, respectively. Therefore the MA cations carry a Born charge monopole term $Z^{\mathrm{mono}}_{\mathrm{MA}} = 0.42 + 0.70 = 1.12$, as well as an effective dipole with charge $|Z^{\mathrm{dip}}_{\mathrm{MA}}| = 0.56$. If we take the C$-$N bond length as the dipole length we obtain an 'effective dipole' of 3.9 D, which is about twice the dipole of a water molecule.

We also note that the total isotropic Born charge of the PbI_3 network is -1.2, and this is compensated by the total charge of each cation +1.2. The fact that these values are close to the nominal charges indicates that the covalent interaction between these two components is essentially negligible.

As a sanity check we verified that the total Born effective charge tensor of the unit cell is (almost) vanishing: we find the largest component to be $\max_{\kappa,\alpha\beta}\sum_\kappa Z^*_{\kappa,\alpha\beta} = 0.17$ when using a 4×4×4 Brillouin zone sampling, and an even smaller value of 0.09 when using a 6×6×6 sampling. These values can be considered as negligible given that there are 48 atoms in the unit cell. The calculated Born effective charges are summarized in Table 5.

3.6 Calculated infrared absorption spectrum

In order to calculate the IR absorption spectrum, we consider the fact that in our experiment the spectrum is measured at normal incidence. With this experimental geometry only TO normal modes can be excited. Therefore we determine the IR spectrum of $MAPbI_3$ using the calculated

TO normal modes. Our results are shown in Figure 7(b), (d), and (f). Moving from high frequency to low frequency in Fig. 7(f), the two peaks with the highest intensity around 3084 cm^{-1} and 3067 cm^{-1} correspond to N−H stretching modes with E symmetry. Right next to these peaks a shoulder appears at lower frequencies, 3046 cm^{-1}. This feature is assigned to C−H and N−H stretching modes with E and A_1 symmetry, respectively.

Now we move to Fig. 7(b). After crossing a gap of almost 1500 cm^{-1} we find the next peak at 1536 cm^{-1}, which corresponds to NH_3 bending modes with E symmetry. Immediately next we have two peaks, at 1418 and 1399 cm^{-1}, and a small feature at 1366 cm^{-1}. The first peak originates from NH_3 bending modes of A_1 symmetry, and the second is from CH_3 bending with E symmetry. The small feature is also from CH_3 bending, this time with A_1 symmetry. The features with very small IR intensities at 1232 and 1026 cm^{-1} correspond to E-symmetry $CH_3NH_3^+$ rocking modes and A_1-symmetry C−N stretching modes, respectively. Proceeding toward lower frequencies we find two peaks at 906 and 890 cm^{-1}, both corresponding to rocking modes of the $CH_3NH_3^+$ with E symmetry. Our assignment is similar to that reported in by Glaser et al.[45] and Carpentier et al.[73] Turning our attention to Fig. 7(d) we see two peaks at 170 and 150 cm^{-1} with significant IR intensity. These peaks originate from the librations of the MA cations. We also find a very small activity for one spinning mode of the cations, at 127 cm^{-1}. The peaks between 10 and 100 cm^{-1} originate from vibrations of the PbI_3 network with B_u symmetry. In particular the peak at 58 cm^{-1} is comprised of several Pb−I stretching modes with B_{1u}, B_{2u} and B_{3u} symmetry.

Overall the present analysis indicates that the IR spectrum of $MAPbI_3$ can be partitioned in three well-distinct regions: the internal vibrations of the MA cations between 800−3100 cm^{-1}, the librations of MA cations in the range 140−180 cm^{-1}, and the internal vibrations of the PbI_3 network below 140 cm^{-1}.

The IR absorption spectrum is closely related to the frequency-dependent dielectric permittivity, therefore we take this opportunity to comment on the permittivity as well. Our calculations yield a high-frequency dielectric constant $\varepsilon_\infty = 5.9$ (the tensor is found to be diagonal and essentially isotropic). This value is in agreement with previous work: Umari et al.[69] calculated a permittivity of 5.5 (7.6) within a DFT (GW) framework. In addition, the measured dielectric constant of $MAPbI_3$ at high-frequency is 6.5.[74] Figure 8 shows the calculated frequency-dependent permittivity $\epsilon(\omega)$ in the infrared spectral range (we consider the isotropic average since the tensor is practically isotropic).

The static permittivity is found to be $\varepsilon_0 = 25.3$, in reasonable agreement with the experimental value of 30.5 at 126 K reported by Poglitsch and Weber.[32] We found that the most important contributions to the dielectric screening arise from the Pb−I stretching modes of B_u symmetry at 61.5, 59.7, 57.9 and 54.4 cm^{-1}, and from the Pb−I−Pb rocking modes of B_u symmetry at 35.2, 33.4, 33.1 and 31.3 cm^{-1}. The contributions of these modes are highlighted in Fig. 8.

4 Comparison between theory and experiment

The experimentally measured IR absorbance spectrum over a wide range of energies from 6 cm^{-1} to 3500 cm^{-1} is presented in Figure 7(a). As predicted by theory, thee distinct groups of absorption peaks are observed. The slowly oscillating background in the experimental absorbance spectrum is an interference artifact associated with highly flat evaporated $MAPbI_3$ film creating a Fabry-Perot cavity for transmitted IR radiation. The comparison between the measured and the calculated IR spectra of $MAPbI_3$ in the low-temperature *Pnma* structure is satisfactory throughout the wide frequency range from 10 cm^{-1} to over 3500 cm^{-1} (i.e. almost up to 0.4 eV), both in terms of peak frequencies and intensities. Figure 7 shows that the best agreement between theory and experiment is obtained in the central portion of the spectrum for the internal vibrations of the cations. In this frequency range, the assignment of the experimental peaks is quite natural, and the result is shown in Fig. 7(a)-(b) (dashed blue lines). In the high-frequency region of the spectrum, we have the H-related stretching vibrations, and here the deviation between theory and experiment is more pronounced ($\sim$70 cm^{-1}). As we can see from Table 4 this deviation is associated with our use of the LDA functional, and a PBE calculation would lead to a significantly better agreement with experiment. Based on Table 4 we can safely assign the measured peaks by assuming that a more accurate calculation would rigidly shift the theoretical spectrum towards higher frequencies. The resulting assignment is shown in Fig. 7(e)-(f). For the low-frequency region of the spectrum, corresponding to the librations of the cations and to the internal vibrations of the PbI_3 network, the comparison between theory and experiment indicates a good agreement, except for an additional peak around 150 cm^{-1} in the calculated spectrum. In the measured spectrum we clearly recognize four prominent peaks and two smaller features [marked by dashes in Fig. 7(c)]; in the theoretical spectrum we have a prominent peak at 58 cm^{-1}, a hump between 140 and 190 cm^{-1}, and two low

intensities features at 30 and 80 cm^{-1}. By trying to match frequency and intensity of each peak we tentatively propose the assignment shown by the blue dashed lines in Fig. 7(c)-(d).

In the case of the librational modes of the cations, our calculations appear to overestimate the energy of the measured peaks by as much as 100 cm^{-1}. Our present results agree with previous calculations reporting significant IR intensity in the range 140–180 cm^{-1}.[44] We performed systematic tests to see whether this is an effect of calculation parameters. As shown in Table 4, the overestimation is significantly reduced (by as much as 30%) when van der Waals corrections are included in our calculations. This result indicates that the interactions between the H atoms of the MA cations and the PbI_3 network may affect the frequency of the libration modes of the MA cations. A much better agreement is obtained for the internal vibrations of the PbI_3. The prominent peak and the two low intensities features of the calculated spectrum can be clearly assigned to the two lowest-frequency peaks and the two satellites of the measured IR spectrum, respectively.

In Table 6 we provide a summary of our *tentative* assignment of the features of the measured IR spectrum of $MAPbI_3$, labelled $P_0,\ldots,P_{18}$. In particular we propose the following attribution: P_0 (17 cm^{-1}) is a Pb−I−Pb rocking mode of B_u symmetry; P_1 and P_2 (22 cm^{-1} and 30 cm^{-1}, respectively) are Pb−I stretching modes of B_u symmetry; P_3 (35 cm^{-1}) is a Pb−I−Pb bending mode of B_u symmetry; P_4 and P_5 (47 cm^{-1} and 59 cm^{-1}, respectively) are libration/translation modes of the MA cations; P_6 and P_7 (906 cm^{-1} and 919 cm^{-1}, respectively) are CH_3NH_3 rocking modes of E symmetry; P_8 (968 cm^{-1}) is a C−N stretching mode of A_1 symmetry; P_9 (1255 cm^{-1}) is a CH_3NH_3 rocking mode of symmetry E; P_{10} and P_{11} (1386 cm^{-1} and 1419 cm^{-1}, respectively) are CH_3 bending modes of symmetry A_1; P_{12} (1450 cm^{-1}) is a CH_3 bending mode of E symmetry; P_{13} (1457 cm^{-1}) is a NH_3 bending mode of A_1 symmetry; P_{14} (1586 cm^{-1}) is NH_3 bending mode of E symmetry; P_{15} (3030 cm^{-1}) is C−H stretching mode of A_1 symmetry; P_{16} (3080 cm^{-1}) is comprised of a C−H stretching mode of E symmetry and a N−H stretching mode of A_1 symmetry; P_{17} (3124 cm^{-1}) is a N−H stretching mode of E symmetry; P_{18} (3172 cm^{-1}) is a N−H stretching mode of E symmetry.

4.1 Low-temperature vs. room-temperature spectra

It is instructive to compare our IR spectrum of the low-temperature phase (orthorhombic) of the $MAPbI_3$ perovskite with the data for the room-temperature phase (tetragonal) reported in the

literature. We find that in the high-frequency region there are peaks in the IR spectrum of the orthorhombic phase which remain distinguishable in the tetragonal phase, while other peaks merge into broad structures at high temperature. For instance, the peaks at 3172 and 3124 cm^{-1} (N-H stretching modes) in our experimental IR spectrum can clearly be recognized in the spectrum of the room-temperature phase measured by Glaser et al.[45], approximately at the same frequencies, 3179 and 3132 cm^{-1}, respectively. The same behavior is observed for our measured peak at 968 cm^{-1} corresponding to the C-N stretching mode of the MA cations. Glaser et al.[45] and Onoda-Yamamuro et al.[43] measured this normal mode at 960 and 961 cm^{-1}, respectively. Onoda-Yamamuro et al.[43] also found that in the IR spectrum of the orthorhombic phase there are two sharp peaks with frequencies at 907 and 917 cm^{-1}, which merge into a single broad peak in the tetragonal phase. Interestingly, we observe the two sharp peaks of the orthorhombic phase in our IR spectrum. They appear at 906 and 9019 cm^{-1} and are assigned to CH_3NH_3 rocking modes. Probably a similar change takes place for the sharp peaks at 1450 and 1457 cm^{-1} in our infrared spectrum (assigned to CH_3 and NH_3 bending modes, respectively), because in the IR spectrum of the tetragonal phase reported by Glaser et al.[45] only a single broad peak is observed.

We confirm these observations by measuring the infrared spectrum of $MAPbI_3$ at room temperature. In Figure 9 we compare the experimental infrared spectra of the low-temperature and the room-temperature phase of the $MAPbI_3$. Regarding the low-frequency region, we find that the two peaks assigned to MA librations in our infrared spectrum of the orthorhombic phase merge into a single broad peak in the spectrum of the tetragonal phase (see Figure 9), and that a similar change takes place for the two main peaks assigned to the internal vibrations of the PbI_3 network. We note that in the low-frequency region our experimental infrared spectrum of the room-temperature phase is rather different from the one reported by Mosconi et al.[44] These authors report significant infrared activity between 100 and 300 cm^{-1}, however, in our experimental data there are no peaks between 100 and 800 cm^{-1}. The origin of the additional structure in the spectra of Mosconi et al.[44] remains an open question, and it might possibly relate to impurities or photo-induced structural changes.

4.2 LO-TO splitting

By calculating the non-analytical part of the dynamical matrix we find that TO and LO frequencies of most normal modes are very close, their differences being smaller than 3–7 cm^{-1} throughout the

entire frequency range. One notable exception is a normal mode of the PbI_3 network with B_{2u} symmetry, which exhibits a LO-TO splitting of 50 cm^{-1}. The calculated TO and LO frequencies of this mode are 53.6 cm^{-1} (this is an average over two B_{2u} modes of similar frequencies) and 104.5 cm^{-1}, respectively. This LO-TO doublet is clearly visible in Fig. 10 (marked by the vertical black bars). Since the calculated frequency of the TO mode labelled as P_2 in Fig. 7 underestimates the measured frequency by approximately 23.6 cm^{-1}, we expect the corresponding LO mode to appear around $\sim 104.5 + 23.6 = 128.1$ cm^{-1} in the experimental spectra. In this crude estimate we assumed that the calculated LO-TO splitting is the same in theory and experiment.

5 Conclusions

In conclusion, we performed a joint computational and experimental study of the infrared absorption spectrum of the hybrid halide perovskite $CH_3NH_3PbI_3$. We reported a detailed analysis of the vibrational eigenmodes and eigenfrequencies calculated within density functional perturbation theory, including a comprehensive factor group analysis. We also calculated the IR intensities and the IR spectrum of this compound in the low-temperature orthorhombic *Pnma* structure. Our analysis indicates that the IR spectrum of $MAPbI_3$ consists of three regions, namely the vibrations of the MA cations (800−3100 cm^{-1}), the librations of the cations, (140−180 cm^{-1}), and the internal vibrations of the PbI_3 network (< 140 cm^{-1}). The static dielectric constant, which is calculated to be $\epsilon_0 = 25.3$, is dominated by contributions from the B_u Pb−I stretching and Pb−I−Pb rocking modes of the PbI_3 network with frequencies below 110 cm^{-1}.

We performed IR measurements at 10 K on evaporated perovskite films and obtained spectra of $MAPbI_3$ over a wide frequency range from 6–3500 cm^{-1}. By comparing the calculated and measured spectra we succeeded in assigning a number of prominent spectral features. We identified three distinct regions in the spectra: the stretching and bending vibrations of the PbI_3 network below 140 cm^{-1}, the librations of the MA cations in the range 140−180 cm^{-1}, and the stretching, bending, and rocking modes of the MA cations between 800−3100 cm^{-1}. In particular we identified the two main peaks at low frequency as Pb−I stretching modes of B_u symmetry (22 and 30 cm^{-1}) and MA librational modes (47 and 59 cm^{-1}). Our assignments will prove helpful in future characterization of these compounds using infrared spectroscopy.

Future work will be needed to clarify the origin of the theoretical overestimation of the librational frequencies. Even after a careful sensitivity analysis we did not succeed in identifying the origin of this discrepancy between theory and experiment. The inclusion of van der Waals interactions brings the calculated frequencies closer to experiment, but the overestimation remains significant. This finding calls for more detailed investigations into the role of van der Waals interactions in the librational modes of the MA cations.

From our factor group analysis we were able to correctly predict the IR activity of the modes. In addition we made predictions for the Raman activity of each vibrational mode, and we noted agreement with previously reported Raman spectra. Given that we developed a complete symmetry analysis of vibrational modes in $MAPbI_3$, it would be interesting to see additional high-resolution Raman measurements in order to complete our understanding of the infrared activity of these important compounds.

We hope that the present work will stimulate further studies on the lattice dynamics and dielectric properties of $MAPbI_3$ and related organometal halide perovskites.

Acknowledgement

This work was supported by the UK Engineering and Physical Sciences Research Council (Grant Numbers EP/J009857/1 and EP/L024667/1), the Leverhulme Trust (Grant RL-2012-001), the European Research Council (EU FP7 / ERC grant no. 239578); the research leading to these results has received funding from the European Union Seventh Framework Programme under grant agreement n° 604391 Graphene Flagship. This work used the ARCHER UK National Supercomputing Service via the AMSEC Leadership project, and the Advanced Research Computing facility of the University of Oxford. All structural models were rendered using VESTA.[75]

References

(1) Best Research-cell Efficiencies. `http://www.nrel.gov/ncpv`, 2014.

(2) Kojima, A.; Teshima, K.; Shirai, Y.; Miyasaka, T. Organometal Halide Perovskites as Visible-Light Sensitizers for Photovoltaic Cells. *J. Am. Chem. Soc.* **2009**, *131*, 6050–6051.

(3) Kim, H.-S.; Lee, C.-R.; Im, J.-H.; Lee, K.-B.; Moehl, T.; Marchioro, A.; Moon, S.-J.; Humphry-Baker, R.; Yum, J.-H.; Moser, J. E.; Grätzel, M.; Park, N.-G. Lead Iodide Perovskite Sensitized All-Solid-State Submicron Thin Film Mesoscopic Solar Cell with Efficiency Exceeding 9%. *Sci. Rep.* **2012**, *2*, 591.

(4) Lee, M. M.; Teuscher, J.; Miyasaka, T.; Murakami, T. N.; Snaith, H. J. Efficient Hybrid Solar Cells Based on Meso-Superstructured Organometal Halide Perovskites. *Science* **2012**, *338*, 643–647.

(5) Ball, J. M.; Lee, M. M.; Hey, A.; Snaith, H. J. Low-Temperature Processed Meso-Superstructured to Thin-Film Perovskite Solar Cells. *Energy Environ. Sci.* **2013**, *6*, 1739–1743.

(6) Liu, M.; Johnston, M. B.; Snaith, H. J. Efficient Planar Heterojunction Perovskite Solar Cells by Vapour Deposition. *Nature* **2013**, *501*, 395–398.

(7) Liu, D.; Kelly, T. L. Perovskite Solar Cells with a Planar Heterojunction Structure Prepared Using Room-Temperature Solution Processing Techniques. *Nature Photonics* **2014**, *8*, 133–138.

(8) Chen, Q.; Zhou, H.; Hong, Z.; Luo, S.; Duan, H.-S.; Wang, H.-H.; Liu, Y.; Li, G.; Yang, Y. Planar Heterojunction Perovskite Solar Cells Via Vapor-Assisted Solution Process. *J. Am. Chem. Soc.* **2014**, *136*, 622–625.

(9) He, M.; Zheng, D.; Wang, M.; Lin, C.; Lin, Z. High Efficiency Perovskite Solar Cells: from Complex Nanostructure to Planar Heterojunction. *J. Mater. Chem. A* **2014**, *2*, 5994.

(10) Bai, S.; Wu, Z.; Wu, X.; Jin, Y.; Zhao, N.; Chen, Z.; Mei, Q.; Wang, X.; Ye, Z.; Song, T.; Liu, R.; Lee, S.-t.; Sun, B. High-Performance Planar Heterojunction Perovskite Solar Cells:

Preserving Long Charge Carrier Diffusion Lengths and Interfacial Engineering. *Nano Research* *7*, 1749.

(11) Gamliel, S.; Etgar, L. Organo-Metal Perovskite Based Solar Cells: Sensitized Versus Planar Architecture. *RSC Adv.* **2014**, *4*, 29012.

(12) Docampo, P.; Ball, J. M.; Darwich, M.; Eperon, G. E.; Snaith, H. J. Efficient Organometal Trihalide Perovskite Planar-Heterojunction Solar Cells on Flexible Polymer Substrates. *Nature Commun.* **2013**, *4*, 2761.

(13) Kumar, M. H.; Yantara, N.; Dharani, S.; Grätzel, M.; Mhaisalkar, S.; Boix, P. D.; Mathews, N. Flexible, Low-Temperature Solution Processed ZnO-Based Solar Cells. *Chem. Commun.* **2013**, *49*, 11089.

(14) You, J.; Hong, Z.; Yang, Y. M.; Chen, Q.; Cai, M.; Song, T.-B.; Chen, C.-C.; Lu, S.; Liu, Y.; Zhou, H.; Yang, Y. Low-Temperature Solution-Processed Perovskite Solar Cells with High Efficiency and Flexibility. *ACS Nano* **2014**, *8*, 1674.

(15) Roldan-Carmona, C.; Malinkiewicz, O.; Soriano, A.; Espallargas, G. M.; Garcia, A.; Reinecke, P.; Kroyer, T.; Dar, M. I.; Nazeeruddin, M. K.; Bolink, H. J. Flexible High Efficiency Solar Cells. *Energy Environ. Sci.* **2014**, *7*, 994–997.

(16) Eperon, G. E.; Burlakov, V. M.; Goriely, A.; Snaith, H. J. Neutral Color Semitransparent Microstructured Perovskite Solar Cells. *ACS Nano* **2014**, *8*, 591.

(17) Roldan-Carmona, C.; Malinkiewicz, O.; Betancur, R.; Longo, G.; Momblona, C.; Jaramillo, F.; Bolink, H. J. High Efficiency Single-Junction Semitransparent Solar Cells. *Energy Environ Sci.* **2014**, *7*, 2968–2973.

(18) Noh, J. H.; Im, S. H.; Heo, J. H.; Mandal, T. N.; Seok, S. I. Chemical Management for Colorful, Efficient, and Stable Inorganic-Organic Hybrid Nanostructured Solar Cells. *Nano Lett.* **2013**, *13*, 1764–1769.

(19) Eperon, G. E.; Stranks, S. D.; Menelaou, C.; Johnston, M. B.; Herz, L. M.; Snaith, H. J. Formamidinium Lead Trihalide: a Broadly Tunable Perovskite for Efficient Planar Heterojunction Solar Cells. *Energy Environ. Sci.* **2014**, *7*, 982–988.

(20) Kulkarni, S. A.; Baikie, T.; Boix, P. P.; Yantara, N.; Mathews, N.; Mhaisalkar, S. Band-Gap Tuning of Lead Halide Perovskites Using a Sequential Deposition Process. *J. Mater. Chem. A* **2014**, *2*, 9221.

(21) Green, M.; Ho-Baillie, A.; Snaith, H. J. The Emergence of Perovskite Solar Cells. *Nature Photonics* **2014**, *8*, 506.

(22) Baikie, T.; Fang, Y.; Kadro, J. M.; Schreyer, M.; Wei, F.; Mhaisalkar, S. G.; Graetzel, M.; White, T. J. Synthesis and Crystal Chemistry of the Hybrid Perovskite $(CH_3NH_3)PbI_3$ for Solid-State Sensitized Solar Cell Applications. *J. Mater. Chem. A* **2013**, *1*, 5628–5641.

(23) D'Innocenzo, V.; Grancini, G.; Alcocer, M. J. P.; Kandada, A. R. S.; Stranks, S. D.; Lee, M. M.; Lanzani, G.; Snaith, H. J.; Petrozza, A. Excitons Versus Free Charges in Organo-Lead Tri-Halide Perovskites. *Nature Commun.* **2014**, *5*, 3586.

(24) Stranks, S. D.; Eperon, G. E.; Grancini, G.; Menelaou, C.; Alcocer, M. J. P.; Leijtens, T.; Herz, L. M.; Petrozza, A.; Snaith, H. J. Electron-Hole Diffusion Lengths Exceeding 1 Micrometer in an Organometal Trihalide Perovskite Absorber. *Science* **2013**, *342*, 341–344.

(25) Wehrenfenig, C.; Eperon, G. E.; Johnston, M. B.; Snaith, H. J.; Herz, L. M. High Charge Carrier Mobilities and Lifetimes in Organolead Trihalide Perovskites. *Adv. Mater.* **2013**, *26*, 1584.

(26) Xing, G.; Mathews, N.; Sun, S.; Lim, S. S.; Lam, Y. M.; Grätzel, M.; Mhaisalkar, S.; Sum, T. C. Long Range Balanced Electron- and Hole-Transport Lengths in Organic-Inorganic $CH_3NH_3PbI_3$. *Science* **2013**, *342*, 344.

(27) Wehrenfennig, C.; Liu, M.; Snaith, H. J.; Johnston, M. B.; Herz, L. M. Charge-Carrier Dynamics in Vapour-Deposited Films of the Organolead Halide Perovskite $CH_3NH_3PbI_{3-x}Cl_x$. *Energy Environ. Sci.* **2014**, *7*, 2269–2275.

(28) Glazer, A. M. The Classification of Tilted Octahedra in Perovskites. *Acta. Cryst. B* **1972**, *28*, 3384.

(29) Weller, M. T.; Weber, O. J.; Henry, P. F.; Pumpo, A. M. D.; Hansen, T. C. Complete Structure and Cation Orientation in the Perovskite Photovoltaic Methylammonium Lead Iodide between 100 and 352 K. *Chem. Commun.* **2015**, *51*, 4180–4183.

(30) Stoumpos, C. C.; Malliakas, C. D.; Kanatzidis, M. G. Semiconducting Tin and Lead Iodide Perovskites with Organic Cations: Phase Transitions, High Mobilities, and Near-Infrared Photoluminescent Properties. *Inorg. Chem.* **2013**, *52*, 9019–9038.

(31) Wehrenfennig, C.; Liu, M.; Snaith, H. J.; Johnston, M. B.; Herz, L. M. Charge Carrier Recombination Channels in the Low-Temperature Phase of Organic-Inorganic Lead Halide Perovskite Thin Films. *APL Mater.* **2014**, *2*, 081513.

(32) Poglitsch, A.; Weber, D. Dynamic Disorder in Methylammoniumtrihalogenoplumbates (II) Observed by Millimeter-Wave Spectroscopy. *J. Chem. Phys.* **1987**, *87*, 6373–6378.

(33) Zheng, F.; Tekenaka, H.; Wang, F.; Zoocher, N. Z.; Rappe, A. M. First-Principles Calculation of Bulk Photovoltaic Effect in $CH_3NH_3PbI_3$ and $CH_3NH_3PbI_{3-x}Cl_x$. *J. Phys. Chem. Lett.* **2014**, *6*, 31–37.

(34) Mosconi, E.; Amat, A.; Nazeeruddin, M. K.; Grätzel, M.; De Angelis, F. First-Principles Modeling of Mixed Halide Organometal Perovskites for Photovoltaic Applications. *J. Phys. Chem. C* **2013**, *117*, 13902–13913.

(35) Filippetti, A.; Delugas, P.; Mattoni, A. Radiative Recombination and Photoconversion of Methylammonium Lead Iodide Perovskite by First Principles: Properties of an Inorganic Semiconductor within a Hybrid Body. *J. Phys. Chem. C* **2014**, *118*, 24843.

(36) Geng, W.; Zhang, L.; Zhang, Y.-N.; Lau, W.-M.; Liu, L.-M. First-Principles Study of Lead-Iodide Perovskite Tetragonal and Orthorhombic Phases for Photovoltaics. *J. Phys. Chem. C* **2014**, *118*, 19565.

(37) Frost, J. M.; Butler, K. T.; Brivio, F.; Hendon, C. H.; van Schilfgaarde, M.; Walsh, A. Atomistic Origins of High-Performance in Hybrid Halide Perovskite Solar Cells. *Nano Lett.* **2014**, *14*, 2584–2590.

(38) Frost, J. M.; Butler, K. T.; Walsh, A. Molecular Ferroelectric Contributions to Anomalous Hysteresis in Hybrid Perovskite Solar Cells. *APL Mater.* **2014**, *2*, 081506.

(39) Carignano, M. A.; Kachmar, A.; Hutter, J. Thermal Effects on $CH_3NH_3PbI_3$ Perovskite from AB-Initio Molecular Dynamics Simulations. *J. Phys. Chem. C* **2015**,

(40) Wehrenfennig, C.; Liu, M.; Snaith, H. J.; Johnston, M. B.; Herz, L. M. Homogeneous Emission Line Broadening in the Organo Lead Halide Perovskite $CH_3NH_3PbI_{3-x}Cl_x$. *J. Phys. Chem. Lett.* **2014**, *5*, 1300–1306.

(41) Quarti, C.; Grancini, G.; Mosconi, E.; Bruno, P.; Ball, J. M.; Lee, M. M.; Snaith, H. J.; Petrozza, A.; De Angelis, F. The Raman Spectrum of the $CH_3NH_3PbI_3$ Hybrid Perovskite: Interplay of Theory and Experiment. *J. Phys. Chem. Lett.* **2014**, *5*, 279–284.

(42) Ledinský, M.; Löper, P.; Niesen, B.; Holovský, J.; Moon, S.-J.; Yum, J.-H.; De Wolf, S.; Fejfar, A.; Ballif, C. Raman Spectroscopy of Organic-Inorganic Halide Perovskites. *J. Phys. Chem. Lett.* **2015**, *6*, 401–406.

(43) Onoda-Yamamuro, N.; Matsuo, T.; Suga, H. Calorimetric and IR Spectroscopic Studies of Phase Transitions in Methylammonium Trihalogenoplumbates (II). *J. Phys. Chem. Solids* **1990**, *51*, 1383–1395.

(44) Mosconi, E.; Quarti, C.; Ivanovska, T.; Ruani, G.; De Angelis, F. Structural and Electronic Properties of Organo-Halide Lead Perovskites: a Combined IR-Spectroscopy and AB Initio Molecular Dynamics Investigation. *Phys. Chem. Chem. Phys.* **2014**, *16*, 16137–16144.

(45) Glaser, T.; Muller, C.; Sendner, M.; Krekeler, C.; Semonin, O. E.; Hull, T. D.; Yaffe, O.; Owen, J. S.; Kowalsky, W.; Pucci, A.; Lovrincic, R. Infrared Spectroscopic Study of Vibrational Modes in Methylammonium Lead Halide Perovskites. *J. Phys. Chem. Lett.* **2015**, *6*, 2913–2918.

(46) Dove, M. T. *Structure and Dynamics. An Atomic View of Materials*; Oxford University Press, Oxford, 2012.

(47) Gonzalez, R. J.; Zallen, R.; Berger, H. Infrared Reflectivity and Lattice Fundamentals in Anatase TiO_{2}s. *Physical Review B* **1997**, *55*, 7014–7017.

(48) Huang, L.-y.; Lambrecht, W. R. L. Lattice Dynamics in Perovskite Halides $\mathrm{CsSn}{X}_{3}$ with $X=\mathrm{I}, \mathrm{Br}, \mathrm{Cl}$. *Physical Review B* **2014**, *90*, 195201.

(49) Giannozzi, P. et al. QUANTUM ESPRESSO: a Modular and Open-Source Software Project for Quantum Simulations of Materials. *J. Phys.: Condens. Matter* **2009**, *21*, 395502.

(50) Perdew, J. P.; Zunger, A. Self-Interaction Correction to Density-Functional Approximations for Many-Electron Systems. *Phys. Rev. B* **1981**, *23*, 5048–5079.

(51) Ceperley, D. M.; Alder, B. J. Ground State of the Electron Gas by a Stochastic Method. *Phys. Rev. Lett.* **1980**, *45*, 566–569.

(52) Perdew, J. P.; Burke, K.; Ernzerhof, M. Generalized Gradient Approximation Made Simple. *Phys. Rev. Lett.* **1996**, *77*, 3865–3868.

(53) Vanderbilt, D. Soft Self-Consistent Pseudopotentials in a Generalized Eigenvalue Formalism. *Phys. Rev. B* **1990**, *41*, 7892–7895.

(54) Grimme, S. Semiempirical GGA-Type Density Functional Constructed with a Long-Range Dispersion Correction. *J. Comp. Chem.* **2006**, *27*, 1787–1799.

(55) Barone, V.; Casarin, M.; Forrer, D.; Pavone, M.; Sambi, M.; Vittadini, A. Role and Effective Treatment of Dispersive Forces in Materials: Polyethylene and graphite crystals as test cases. *J. Comp. Chem.* **2009**, *30*, 934–939.

(56) Gonze, X.; Lee, C. Dynamical Matrices, Born Effective Charges, Dielectric Permittivity Tensors, and Interatomic Force Constants from Density-Functional Perturbation Theory. *Phys. Rev. B* **1997**, *55*, 10355–10368.

(57) Born, M.; Huang, K. *Dynamical Theory of Crystal Lattices*; Oxford University Press, Oxford, 1954.

(58) Resta, R.; Vanderbilt, D. *Theory of Polarization: A Modern Approach*; Topics in Applied Physics 105; Springer Berlin Heidelberg, 2007; pp 31–68.

(59) Umari, P.; Pasquarello, A. Ab Initio Molecular Dynamics in a Finite Homogeneous Electric Field. *Phys. Rev. Lett.* **2002**, *89*, 157602.

(60) Souza, I.; Íñiguez, J.; Vanderbilt, D. First-Principles Approach to Insulators in Finite Electric Fields. *Phys. Rev. Lett.* **2002**, *89*, 117602.

(61) Stranks, S. D.; Wood, S. M.; Wojciechowski, K.; Deschler, F.; Saliba, M.; Khandelwal, H.; Patel, J. B.; Elston, S. J.; Herz, L. M.; Johnston, M. B.; Schenning, A. P. H. J.; Debije, M. G.; Riede, M. K.; Morris, S. M.; Snaith, H. J. Enhanced Amplified Spontaneous Emission in Perovskites Using a Flexible Cholesteric Liquid Crystal Reflector. *Nano Letters* **0**, *0*, 0.

(62) Docherty, C. J.; Parkinson, P.; Joyce, H. J.; Chiu, M.-H.; Chen, C.-H.; Lee, M.-Y.; Li, L.-J.; Herz, L. M.; Johnston, M. B. Ultrafast Transient Terahertz Conductivity of Monolayer MoS_2 and WSe_2 Grown by Chemical Vapor Deposition. *ACS Nano* **2014**, *8*, 11147–11153.

(63) Filip, M. R.; Giustino, F. GW Quasiparticle Band Gap of the Hybrid Organic-Inorganic Perovskite $CH_3NH_3PbI_3$: Effect of Spin-Orbit Interaction, Semicore Electrons, and Self-Consistency. *Phys. Rev. B* **2014**, *90*, 245145.

(64) Cotton, F. A. *Chemical Applications of Group Theory*; John Wiley and Sons, USA, 1990.

(65) Yu, P. Y.; Cardona, M. *Fundamentals of Semiconductors. Physics and Materials Properties*; Springer-Verlag, Berlin, 1996.

(66) Even, J.; Pedesseau, L.; Jancu, J.-M.; Katan, C. Importance of Spin-Orbit Coupling in Hybrid Organic/Inorganic Perovskites for Photovoltaic Applications. *J. Phys. Chem. Lett.* **2013**, *4*, 2999.

(67) Menéndez-Proupin, E.; Palacios, P.; Wahnón, P.; Conesa, J. C. Self-Consistent Relativistic Band Structure of the $CH_3NH_3PbI_3$ Perovskite. *Phys. Rev. B* **2014**, *90*, 045207.

(68) Brivio, F.; Butler, K. T.; Walsh, A.; van Schilfgaarde, M. Relativistic Quasiparticle Self-Consistent Electronic Structure of Hybrid Halide Perovskite Photovoltaic Absorbers. *Phys. Rev. B* **2014**, *89*, 155204.

(69) Umari, P.; Mosconi, E.; Angelis, F. D. Relativistic GW Calculations on $CH_3NH_3PbI_3$ and $CH_3NH_3SnI_3$ Perovskites for Solar Cell Applications. *Sci. Rep.* **2014**, *4*, 4467.

(70) Giustino, F. *Materials Modelling Using Density Functional Theory: Properties and Predictions*; Oxford University Press, Oxford, 2014.

(71) Mikami, M.; Nakamura, S.; Kitao, O.; Arakawa, H. Lattice Dynamics and Dielectric Properties of TiO_2 Anatase: a First-Principles Study. *Phys. Rev. B* **2002**, *66*, 155213.

(72) Ghosez, P.; Michenaud, J.-P.; Gonze, X. Dynamical Atomic Charges: the Case of ABO_3 Compounds. *Phys. Rev. B* **1998**, *58*, 6224–6240.

(73) Carpentier, P.; Lefebvre, J.; Jakubas, R. Raman Studies of the Ferroelectric Phase Transitions in $(CH_3NH_3)_5Bi_2Cl_{11}$ (MAPCB). I. The Internal Vibrations of the Methylammonium Cation. *J. Phys.: Condens. Matter* **1992**, *4*, 2985–2999.

(74) Hirasawa, M.; Ishihara, T.; Goto, T.; Uchida, K.; Miura, N. Magnetoabsorption of the Lowest Exciton in Perovskite-Type Compound $(CH_3NH_3)PbI_3$. *Physica B: Condensed Matter* **1994**, *201*, 427–430.

(75) Momma, K.; Izumi, F. *VESTA* : a Three-Dimensional Visualization System for Electronic and Structural Analysis. **2008**, *41*, 653–658.

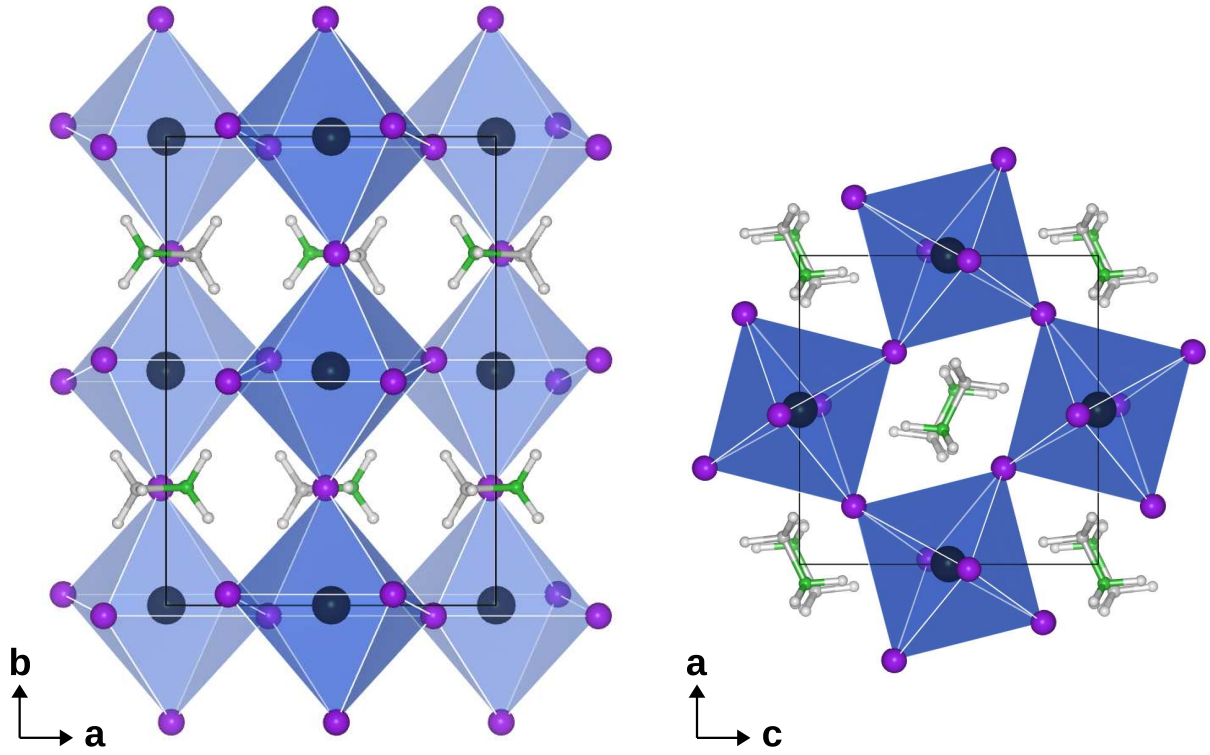

Figure 1: Optimized structure of $MAPb_3$ in the orthorhombic phase. The Pb atoms are represented by the large black spheres in the center of the shaded octahedra. The smaller purple spheres located at the corners of the octahedra indicate the I atoms. The MA cations are represented using ball-and-stick models, with gray, green and white spheres denoting C, N and H atoms, respectively. The unit cell is indicated by the black straight lines, with the axes given at the bottom.

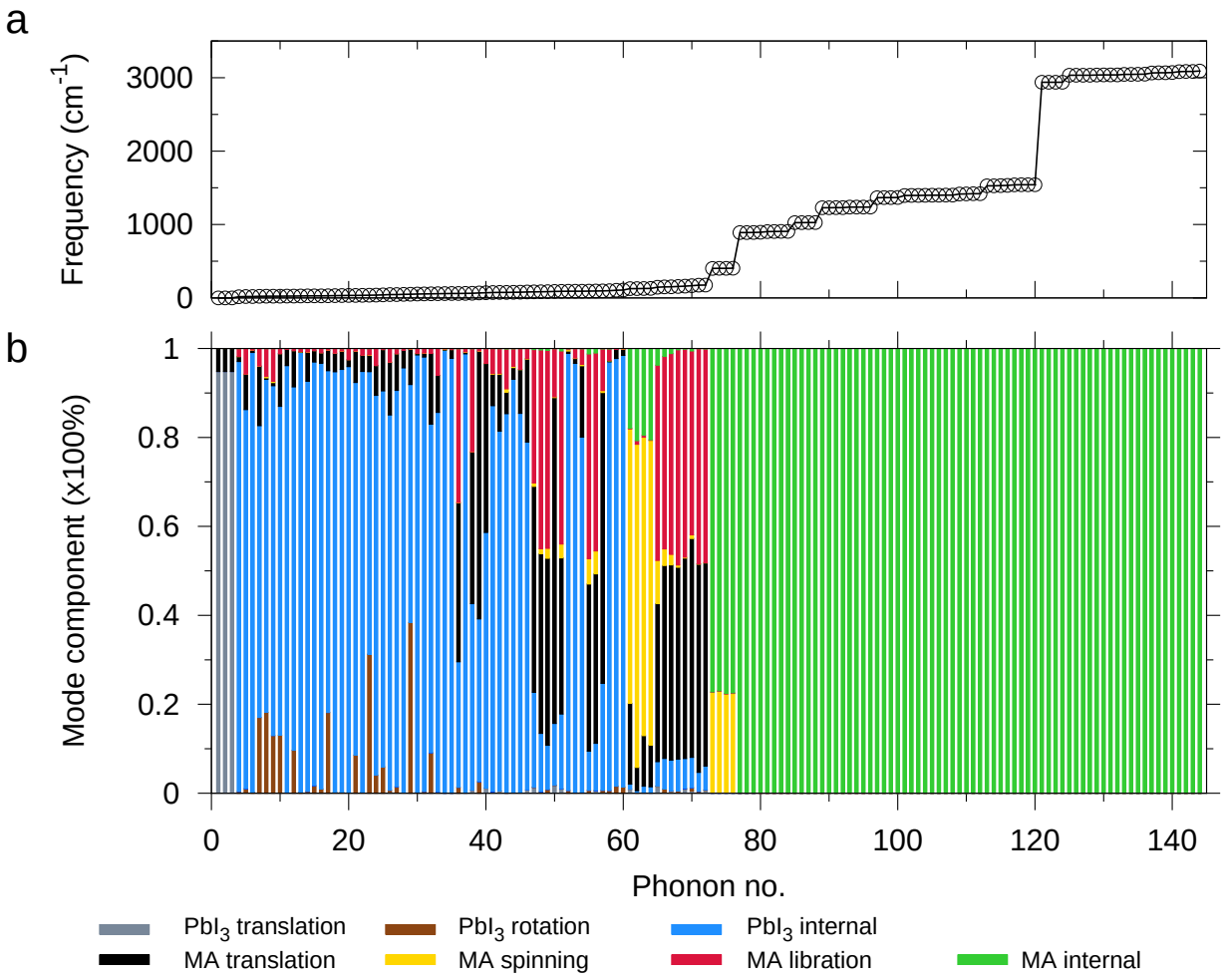

Figure 2: (a) Calculated vibrational frequencies for each eigenmode (discs). The line is a guide to the eye. (b) Decomposition of the vibrational modes of $MAPbI_3$ in the low-temperature orthorhombic phase at the Γ point. The height of each stick represents the contribution of the corresponding vibration to each eigenmode, according to Eq. (6). The color code is indicated in the legend.

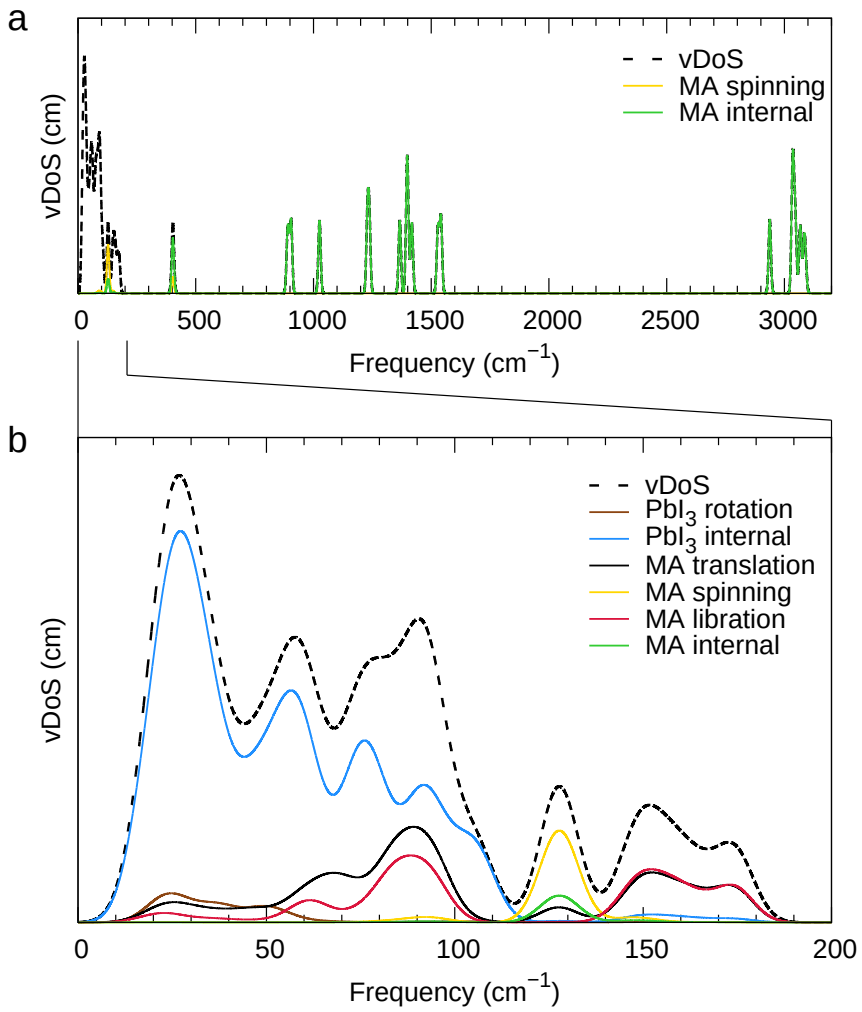

Figure 3: (a) Total and partial vDOS of $MAPbI_3$ over the entire frequency range 0–3000 cm^{-1}. (b) Detail of total and partial vDOS of $MAPbI_3$ in the range 0–200 cm^{-1}. The color code is the same as in Fig. 2: green and blue are for the internal vibrations of MA and PbI_3, respectively; yellow and red are for MA spin and libration, respectively; black and gray are for MA and PbI_3 translations, respectively; brown is for the rotations of the octahedra. The total vDOS is shown as a thin dashed black line. We employed a Gaussian smearing of 5 cm^{-1} throughout.

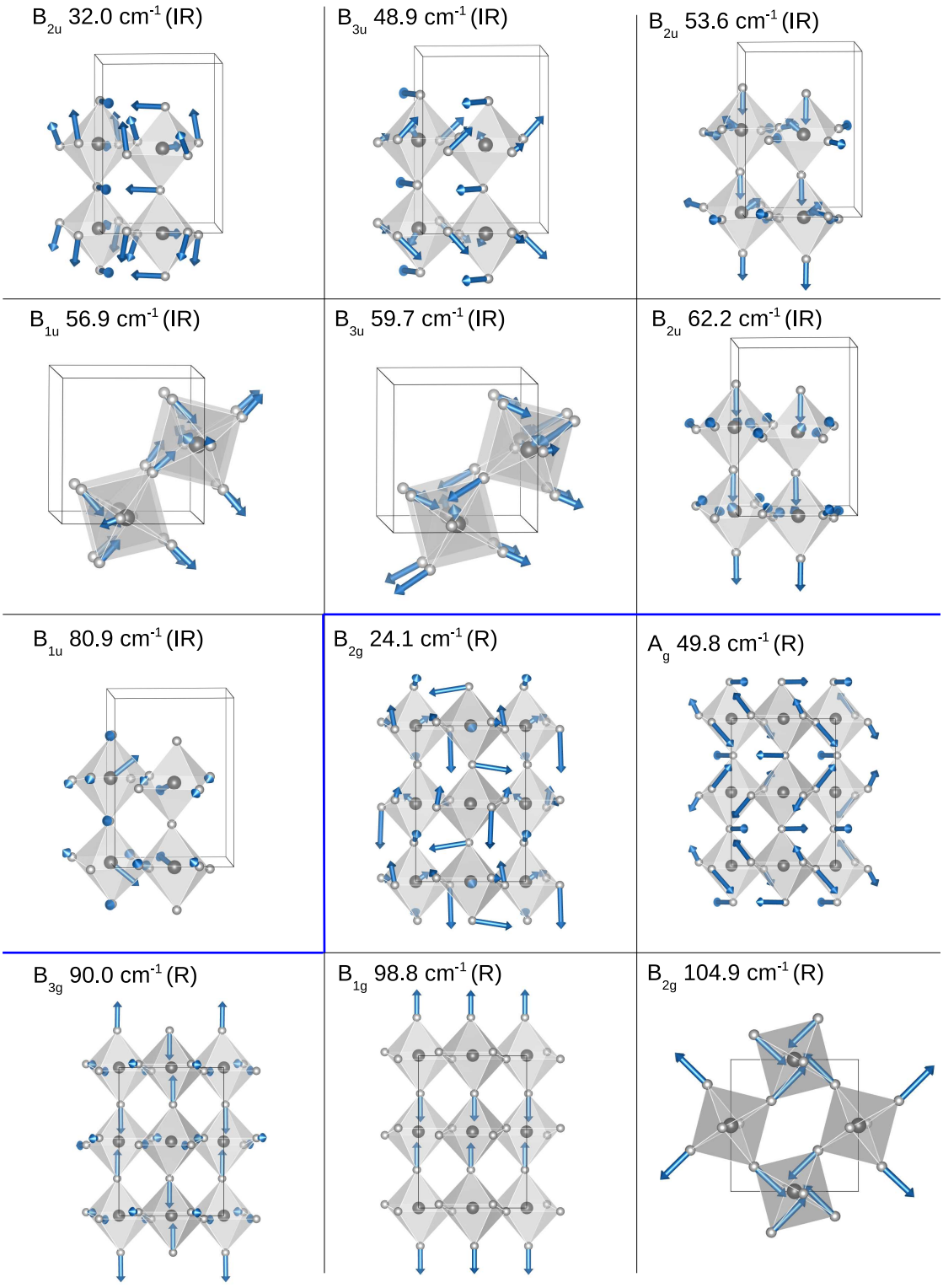

Figure 4: Schematic representation of some representative normal modes of vibration of the PbI_3 network in $MAPbI_3$. The PbI_6 octahedra are shaded, the Pb and I atoms are in black and gray color, respectively, and the MA cations are not shown for clarity. The symmetry, (calculated) frequency and IR or Raman activity of each mode are also indicated.

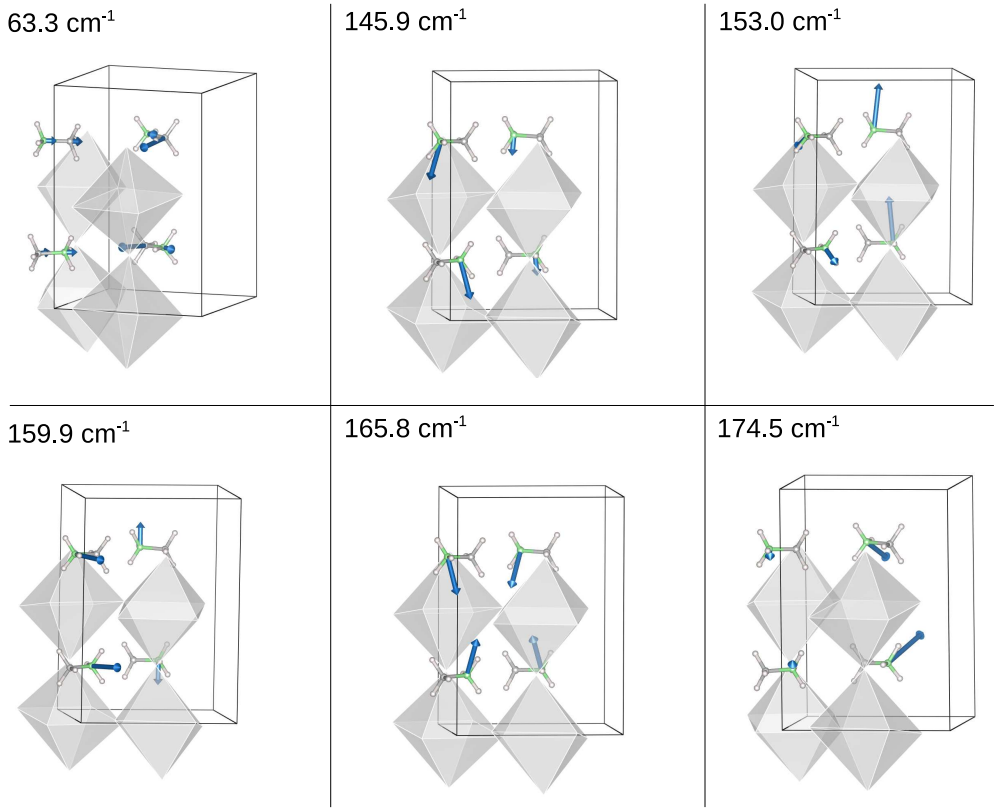

Figure 5: Schematic representation of the vibrational modes of $MAPbI_3$ corresponding to librations/translations of the MA cations. The Pb and I atoms and the displacements of the H atoms are not shown for clarity. The relative contribution of libration and translation to each mode is provided in Fig. 2. The (calculated) frequency of each mode is indicated.

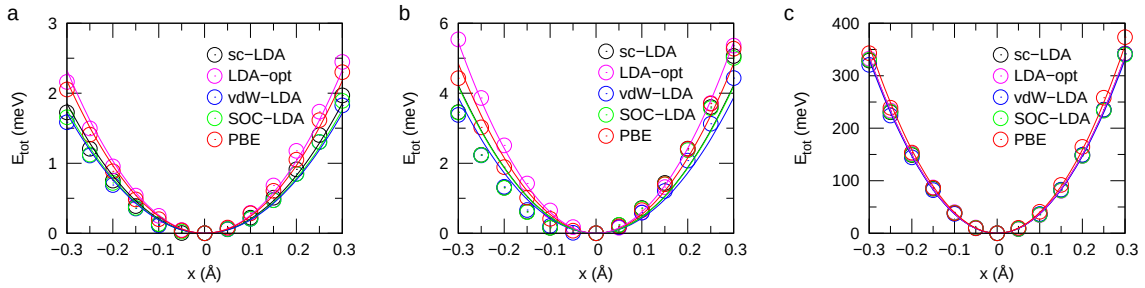

Figure 6: Calculated DFT total energy of one unit cell of $MAPbI_3$ as a function of normal mode coordinate, for (a) the B_{3g} Pb−I stretching mode of the PbI_3 network at 106.9 cm^{-1}, (b) the libration mode of the MA cations at 169 cm^{-1} and (c) the A_1 NH_3 bending mode of the MA cation at 1418 cm^{-1}. The curves refer to: scalar-relativistic LDA calculations with experimental lattice parameters (black circles), scalar-relativistic LDA calculations with optimized lattice parameters (pink open circles), scalar-relativistic LDA with van der Waals interactions (blue open circles), fully relativistic LDA calculations (green filled discs), and scalar-relativistic PBE calculations (red open circles). The lines are parabolic fits and serve as guides to the eye. The vibrational frequencies reported in Table 4 have been obtained as second derivatives of this curves at the minimum.

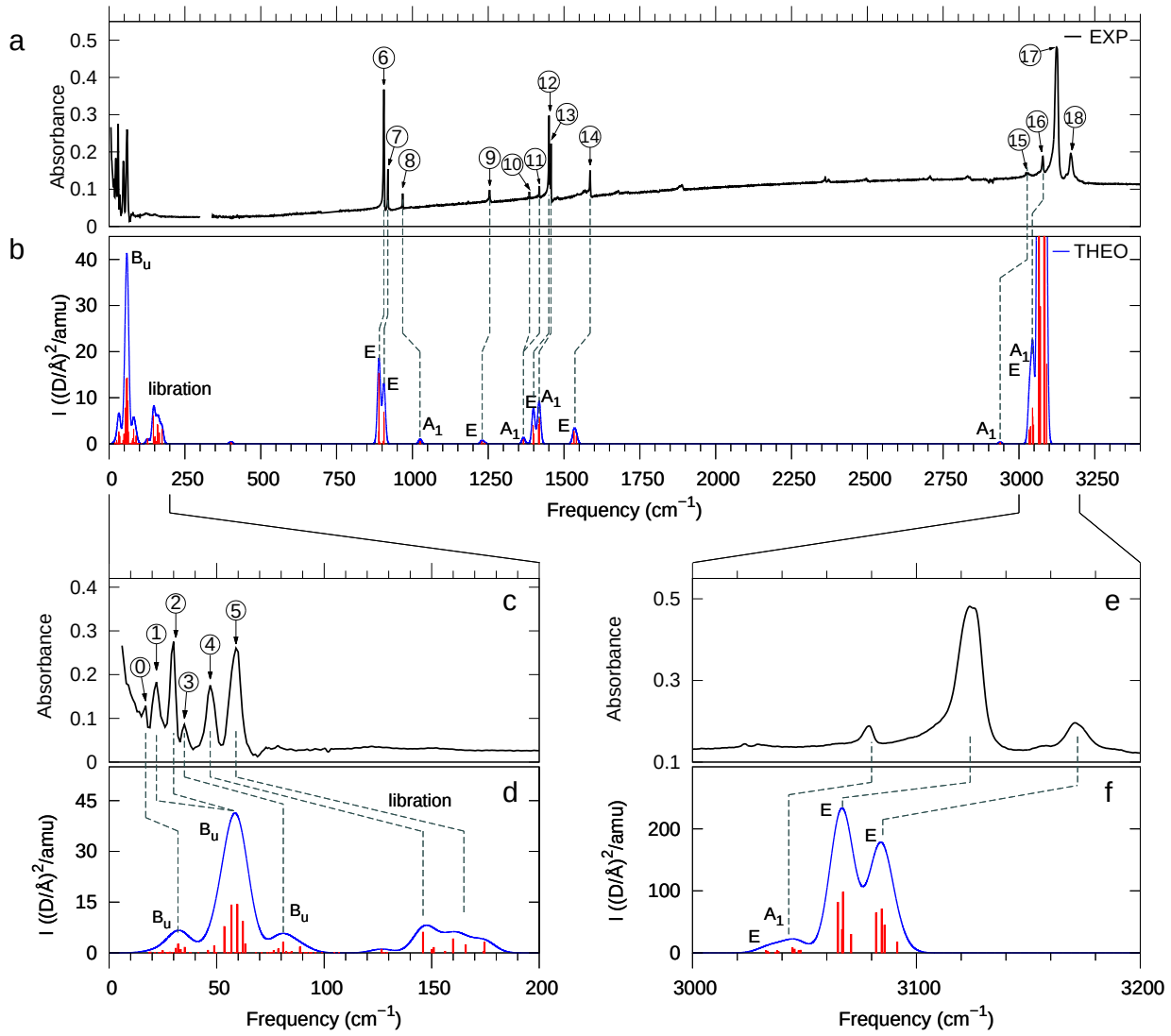

Figure 7: (a) IR spectrum of $MAPbI_3$ measured on thin films at 10 K. The most prominent peaks are labeled by numbers and described in Table 6. The dashed blue lines indicate our tentative assignment of these peaks to the corresponding features in the theoretical spectrum.(b) Calculated IR spectrum of $MAPbI_3$ in the low-temperature orthorhombic phase. The red sticks indicate the calculated IR intensities of each peak, and the blue lines have been obtained using a Gaussian broadening of the sticks. For each mode we indicate the corresponding symmetry, based on the analysis of the normal modes carried out in Sec. 3.3. (c)-(f) Close-up of the experimental and theoretical spectra shown in (a) and (b). The dashes in (c) indicate the peaks discussed in the main text.

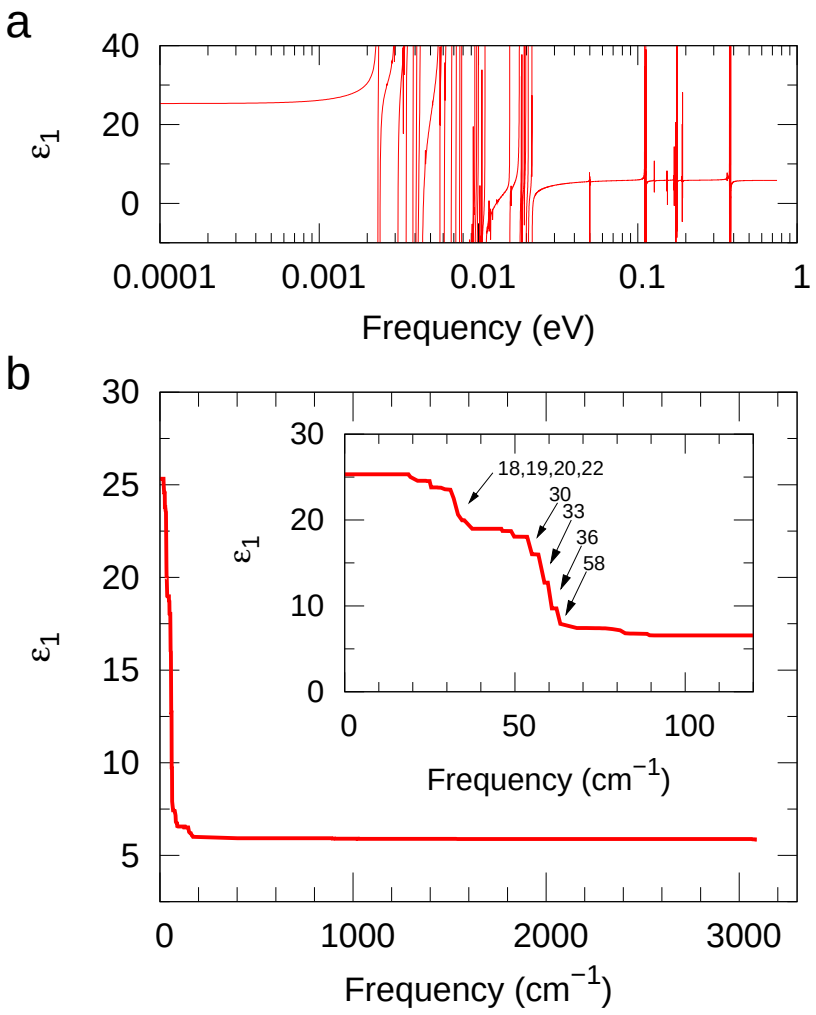

Figure 8: (a) Calculated real part of the frequency-dependent dielectric permittivity of $MAPbI_3$ (note the logarithmic scale on the energy axis). (b) Cumulative contribution of the normal modes to the dielectric permittivity, from the highest to lowest-frequency normal mode. The labels in the inset correspond to the mode numbers in Table 1.

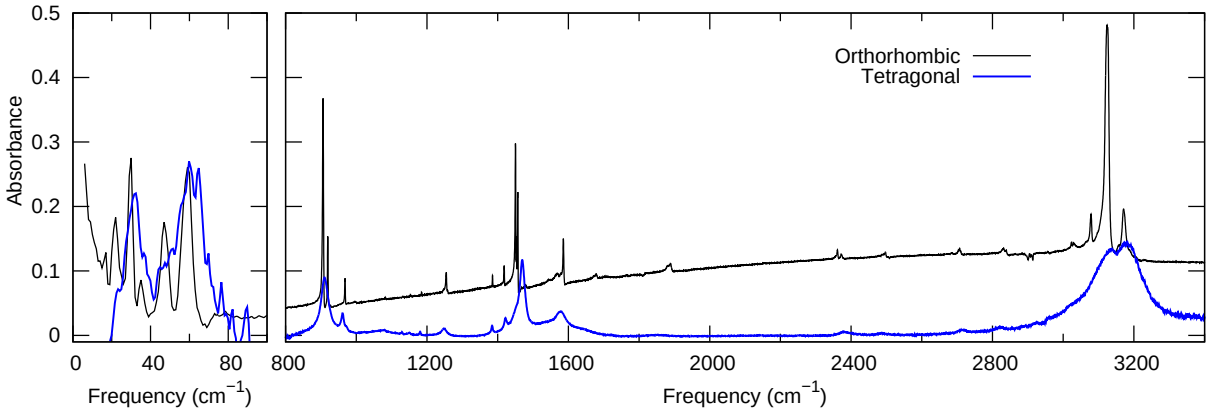

Figure 9: Comparison between the measured infrared spectra of the low-temperature orthorhombic phase (black curve) and the room-temperature tetragonal phase (blue curve) of the $MAPbI_3$ perovskite. The spectra are measured at 10 and 295 K, respectively, at normal incidence. Differences in baseline are due to the fact that the room temperature data is reflection corrected but the low temperature data is not.

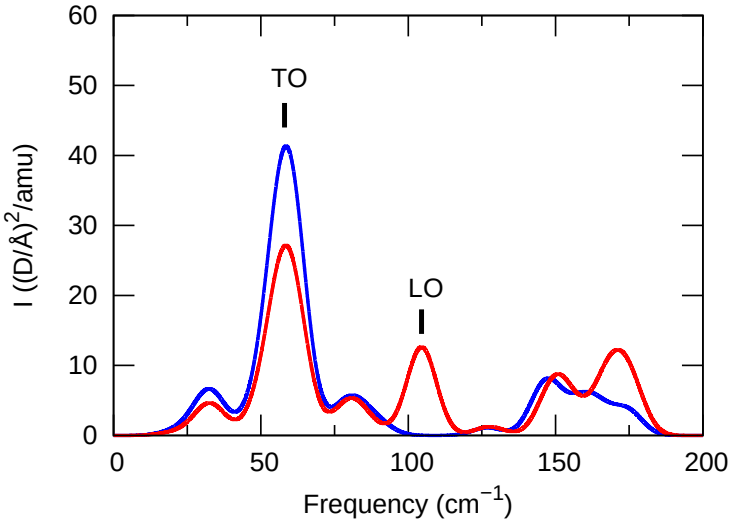

Figure 10: Calculated infrared absorption intensities of $MAPbI_3$ in the low-temperature orthorhombic phase corresponding to the TO modes (blue line) and to the LO modes (red line). For clarity, only the frequency region with the largest LO-TO splitting is shown. The black bars indicate the LO-TO doublet discussed in Sec. 4.2. The infrared activities of the LO modes are calculated for a wavevector along the [111] direction.

Table 1: Symmetry, character and predicted activity of the normal modes of $MAPbI_3$ corresponding to the vibrations of the PbI_3 network. 'IR' and 'R' indicate modes which are expected to be IR-active and Raman-active by symmetry, respectively. We also report the IR intensities calculated from from principles (Sec. 3.6). Whenever the IR intensity is not indicated the value was smaller than 0.1 $(D/Å)^2/amu$.

Mode no.	Symmetry	Character	Active	Frequency (cm^{-1})	IR int. $[(D/Å)^2/amu]$	Mode no.	Symmetry	Character	Active	Frequency cm^{-1}	IR int. $[(D/Å)^2/amu]$
1	B_{1u}			0.0		25	A_g	Pb−I−Pb bend	R	41.6	
2	B_{3u}			0.0		26	B_{1u}	Pb−I−Pb bend	IR	46.2	0.7
3	B_{2u}			0.0		27	B_{3g}	Pb−I−Pb bend	R	46.3	
4	A_u		silent	16.8		28	B_{3u}		IR	48.9	2.1
5	B_{3u}		IR	18.7	0.1	29	A_g	Pb−I−Pb bend	R	49.8	
6	B_{2u}		IR	19.3	0.2	30	B_{2u}	Pb−I stretch	IR	53.6	7.8
7	A_g		R	21.4		31	A_u	Pb−I stretch	silent	55.0	
8	B_{1g}	Pb−I−Pb rock	R	23.1		32	B_{2g}	Pb−I−Pb bend	R	56.2	
9	B_{3g}	Pb−I−Pb rock	R	23.8		33	B_{1u}	Pb−I stretch	IR	56.9	14.1
10	B_{2g}	Pb−I−Pb rock	R	24.1		34	A_u	Pb−I stretch	silent	58.7	
11	B_{1u}		IR	24.9	0.6	35	B_{3u}	Pb−I stretch	IR	59.7	14.3
12	A_u		silent	25.4		37	B_{2u}	Pb−I stretch	IR	62.2	9.3
13	A_u		silent	26.7		41	B_{3u}		IR	73.6	0.1
14	B_{1u}	Pb−I−Pb rock	IR	27.2	0.1	42	B_{1u}		IR	74.9	0.1
15	A_u		silent	27.3		43	A_u		silent	75.6	
16	B_{2u}		IR	28.3	0.2	44	B_{2u}		IR	76.6	0.7
17	A_g	Pb−I−Pb rock	R	29.4		45	B_{3u}		IR	78.7	1.1
18	B_{3u}	Pb−I−Pb rock	IR	31.1	1.3	46	B_{1u}	Pb−I−Pb bend	IR	80.9	3.1
19	B_{2u}		IR	32.0	2.6	52	B_{3g}	Pb−I stretch	R	90.0	
20	B_{3u}	Pb−I−Pb rock	IR	33.3	1.0	53	B_{1g}	Pb−I stretch	R	91.6	
21	B_{2g}	Pb−I−Pb bend	R	34.5		54	A_g	Pb−I stretch	R	91.8	
22	B_{1u}	Pb−I−Pb rock	IR	35.2	1.6	58	B_{1g}	Pb−I stretch	R	98.8	
23	B_{1g}	Pb−I−Pb bend	R	37.4		59	B_{2g}	Pb−I stretch	R	104.9	
24	B_{2g}		R	38.1		60	B_{3g}	Pb−I stretch	R	106.9	

Table 2: Symmetry, character and predicted activity of the normal modes of $MAPbI_3$ corresponding to the vibrations of the MA cations. 'IR' and 'R' indicate modes which are expected to be IR-active and Raman-active by symmetry, respectively. We also report the IR intensities calculated from first principles. The frequencies and intensities have been averaged over degenerate modes.

Mode no.	Symmetry	Character	Active	Frequency (cm^{-1})	IR int. [$(D/Å)^2$/amu]
73–76	A_2	Torsion	silent	402	0.1
77–80	E	CH_3NH_3 rock	IR, R	890	4.6
81–84	E	CH_3NH_3 rock	IR, R	906	3.3
85–88	A_1	C−N stretch	IR, R	1026	0.3
89–96	E	CH_3NH_3 rock	IR, R	1232	0.1
97–100	A_1	sym. CH_3 bend	IR, R	1366	0.3
101–108	E	asym. CH_3 bend	IR, R	1399	1.0
109–112	A_1	sym. NH_3 bend	IR, R	1418	2.4
113–120	E	asym. NH_3 bend	IR, R	1536	0.6
121–124	A_1	sym. C−H stretch	IR, R	2938	0.1
125–132	E	asym. C−H stretch	IR, R	3036	1.7
133–136	A_1	sym. N−H stretch	IR, R	3046	5.1
137–140	E	asym. N−H stretch	IR, R	3067	61.5
141–144	E	asym. N−H stretch	IR, R	3084	49.1

Table 3: Character, frequency, and calculated IR intensity of the vibrational modes corresponding to the rigid-body motion of the MA cations in the orthorhombic $MAPbI_3$ unit cell. We distinguish spin, libration, and translations based on the decomposition in Fig. 1. Modes of mixed character correspond to vibrations where the contribution of different components have similar weights in Fig. 1.

Mode no.	Character	Frequency (cm^{-1})	IR int. [$(D/Å)^2$/amu]	Mode no.	Character	Frequency (cm^{-1})	IR int. [$(D/Å)^2$/amu]
36	libr/transl	60.9		61	spin	126.7	1.0
38	libr/transl	63.3	2.6	62	spin	127.1	
39	translation	68.2		63	spin	128.0	
40	translation	70.9	0.1	64	spin	129.2	
47	libr/transl	82.4	0.3	65	libr/transl	145.9	6.1
48	libr/transl	83.8		66	libr/transl	150.0	1.0
49	libr/transl	84.8	0.3	67	libr/transl	153.0	1.6
50	translation	88.8	1.7	68	libr/transl	156.2	0.4
51	libr/transl	89.5	0.1	69	libr/transl	159.9	4.2
55	libr/transl	93.3		70	libr/transl	165.8	2.4
56	libr/transl	94.0		71	libr/transl	174.2	0.3
57	translation	96.0		72	libr/transl	174.5	3.2

Table 4: Sensitivity of the calculated vibrational frequencies to spin-orbit coupling, lattice parameter, and exchange-correlation functional. We consider the B_{3g} Pb−I stretching mode of the PbI_3 network at 106.9 cm^{-1}, the libration mode of the MA cations at 169 cm^{-1}, and the A_1 NH_3 bending mode of the MA cations at 1418 cm^{-1}. The notation is as follows: DFPT: sc-LDA frequencies obtained from linear response and reported in Table 1 and 2; sc-LDA: scalar-relativistic LDA calculations with experimental lattice parameters; LDA-opt: scalar-relativistic LDA calculations with optimized lattice parameters; vdW-LDA: scalar-relativistic calculations including van der Waals interactions; SOC-LDA: fully relativistic LDA calculations; PBE: scalar-relativistic PBE calculations. The small deviation (< 10 cm^{-1}) between the DFPT and the sc-LDA frequencies is due to the evaluation of the second derivatives via finite differences of the total energy.

	Normal mode		
	B_{3g}	MA libration	A_1
	frequency (cm^{-1})	frequency (cm^{-1})	frequency (cm^{-1})
DFPT	106.9	165.8	1418.0
sc-LDA	105.9	165.9	1421.8
LDA-opt	114.7	176.9	1425.3
vdW-LDA	77.7	143.6	1411.3
SOC-LDA	95.9	153.3	1420.4
PBE	114.7	170.9	1470.4

Table 5: Calculated Born effective charges of $MAPbI_3$ in the low-temperature orthorhombic unit cell. Here we report the isotropic average of the tensors, $\overline{Z}^* = (1/3)\sum_\alpha Z^*_{\alpha\alpha}$. We provide results for each atom, as well as the totals for the PbI_3 network and for the MA cation.

species	$\overline{Z}^*$	species	$\overline{Z}^*$
Pb	+4.42	H_C	+0.13
I	−1.88	H_N	+0.55
C	+0.03	PbI_3	+0.42
N	−0.95	CH_3NH_3	+0.70

Table 6: Tentative assignment of the peaks in the measured IR spectrum of $MAPbI_3$ at 10 K. The peak labels correspond to those indicated in Fig. 7(a).

Mode label	Frequency (cm^{-1})	Symmetry	Description
P_0	17	B_u	Pb−I−Pb rock
P_1	22	B_u	Pb−I stretch
P_2	30	B_u	Pb−I stretch
P_3	35	B_u	Pb−I−Pb bend
P_4	47		Libration/translation
P_5	59		Libration/translation
P_6	906	E	CH_3NH_3 rock
P_7	919	E	CH_3NH_3 rock
P_8	968	A_1	C−N stretch
P_9	1255	E	CH_3NH_3 rock
P_{10}	1386	A_1	CH_3 bend
P_{11}	1419	A_1	CH_3 bend
P_{12}	1450	E	CH_3 bend
P_{13}	1457	A_1	NH_3 bend
P_{14}	1586	E	NH_3 bend
P_{15}	3030	A_1	C−H stretch
P_{16}	3080	E, A_1	C−H stretch, N−H stretch
P_{17}	3124	E	N−H stretch
P_{18}	3172	E	N−H stretch

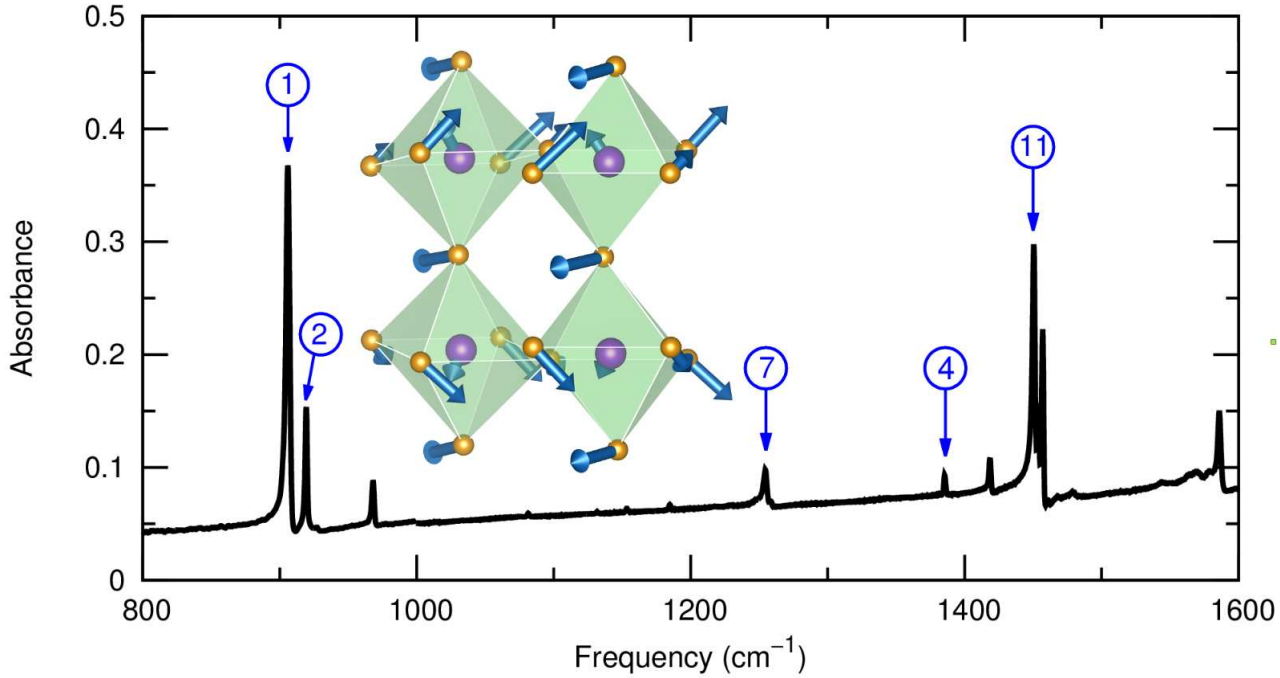

Figure 11: TOC Graphic